

 Open access • Posted Content • DOI:10.1101/2020.10.26.356089

Ancestral circuits for vertebrate colour vision emerge at the first retinal synapse

— [Source link](#) 

Takeshi Yoshimatsu, Philipp Bartel, Cornelius Schröder, F. Janiak ...+5 more authors

Institutions: University of Sussex, University of Tübingen, Baylor College of Medicine, Rice University

Published on: 14 Apr 2021 - bioRxiv (Cold Spring Harbor Laboratory)

Related papers:

- [Zebrafish Differentially Process Color across Visual Space to Match Natural Scenes.](#)
- [Fovea-like Photoreceptor Specializations Underlie Single UV Cone Driven Prey-Capture Behavior in Zebrafish.](#)
- [Near-optimal rotation of colour space by zebrafish cones in vivo](#)
- [Ancestral circuits for vertebrate color vision emerge at the first retinal synapse.](#)
- [Colored visual stimuli evoke spectrally tuned neuronal responses across the central nervous system of zebrafish larvae](#)

Share this paper:    

View more about this paper here: <https://typeset.io/papers/ancestral-circuits-for-vertebrate-colour-vision-emerge-at-2qcdmp1km7>

1 Ancestral circuits for vertebrate colour vision 2 emerge at the first retinal synapse

3 Takeshi Yoshimatsu¹, Philipp Bartel¹, Cornelius Schröder^{2,3}, Filip K Janiak¹, Francois St-
4 Pierre⁴⁻⁶, Philipp Berens^{2,3,7} and Tom Baden^{1,2§}

5
6 **Summary.** For colour vision, retinal circuits separate information about intensity and
7 wavelength. This requires comparison of at least two spectrally distinct
8 photoreceptors, as in the case of most mammals. However, many vertebrates use the
9 full complement of four ‘ancestral’ cone-types (‘red’, ‘green’, ‘blue’, ‘UV’), and in those
10 cases the nature and implementation of this computation remains poorly understood.
11 Here, we establish the complete circuit architecture of outer retinal circuits underlying
12 colour processing in larval zebrafish, which involves the full ancestral complement of
13 four cone- and three horizontal cell types. Our findings reveal that the synaptic
14 outputs of red- and green-cones efficiently rotate the encoding of natural daylight in a
15 principal component analysis (PCA)-like manner to yield primary achromatic and
16 spectrally-opponent axes, respectively. Together, these two cones capture 91.3% of
17 the spectral variance in natural light. Next, blue-cones are tuned so as to capture
18 most remaining variance when opposed to green-cones. Finally, UV-cones present a
19 UV-achromatic axis for prey capture. We note that fruit flies – the only other
20 tetrachromat species where comparable circuit-level information is available - use
21 essentially the same strategy to extract spectral information from their relatively blue-
22 shifted terrestrial visual world. Together, our results suggest that rotating colour
23 space into primary achromatic and chromatic axes at the eye’s first synapse may be a
24 fundamental principle of colour vision when using more than two spectrally well-
25 separated photoreceptor types.

27
28 1, School of Life Sciences, University of Sussex, UK; 2, Institute of Ophthalmic Research, University of Tübingen, Germany; 3:
29 Centre for Integrative Neuroscience, University of Tübingen, Germany; 4: Department of Neuroscience, Baylor College of
30 Medicine, Houston, TX, USA; 5: Department of Electrical and Computer Engineering, Rice University, Houston, TX, USA; 6:
31 Systems, Synthetic, and Physical Biology Program, Rice University, Houston, TX, USA; 7: Institute for Bioinformatics and
32 Medical Informatics, University of Tübingen, Germany.. [§]Correspondence to t.baden@sussex.ac.uk

34 **Acknowledgements.** We thank Sharm Knecht and Rachel Wong for EM volume acquisition. We thank Thomas Euler for
35 critical feedback. The authors would also like to acknowledge support from the FENS-Kavli Network of Excellence and the
36 EMBO YIP.

38 **Author contributions.** TY, PBa and TB designed the study, with input from CS, FKJ and PBe. TY generated novel lines and
39 performed 2-photon data collection and pre-processing. TY also performed anatomical imaging and EM-tracing. TY and CS
40 analysed anatomical data. PBa built the light-stimulator with input from FKJ. PBa and TB performed natural imaging data
41 analysis, with input from PBe. CS performed computational modelling of the HC-cone circuit with input from PBe. CS analysed
42 voltage recordings with input from PBe. CS, TY, PBa and TB performed general statistical analyses, with help from PBe. FSP
43 provided early access to ASAP plasmids. TB wrote the manuscript with inputs from all authors.

45 **Declaration of Interests.** The authors declare no competing interests.

47 **Funding.** Funding was provided by the European Research Council (ERC-StG “NeuroVisEco” 677687 to TB), The Wellcome
48 Trust (Investigator Award in Science 220277/Z20/Z to TB), the UKRI (BBSRC, BB/R014817/1 to TB), the German Ministry for
49 Education and Research (01GQ1601, 01IS18052C, 01IS18039A to PB), the German Research Foundation (BE5601/4-1, EXC
50 2064 – 390727645 to PB), the Leverhulme Trust (PLP-2017-005 to TB), the Lister Institute for Preventive Medicine (to TB).
51 Marie Curie Skłodowska Actions individual fellowship (“ColourFish” 748716 to TY) from the European Union’s Horizon 2020
52 research and innovation programme. FSP was supported by the McNair Medical Foundation, start-up funds from Baylor
53 College of Medicine, the Klingenstein-Simons Fellowship Award in Neuroscience, a Welch Foundation grant (Q-2016-
54 20190330), NIH grants (R01EB027145 and U01NS113294), and NSF grants (NeuroNex 1707359 and IdeasLab 1935265).
55 Sharm Knecht is supported in part by NIH grant (EY01730).

57

INTRODUCTION

58

In visual scenes, information about wavelength is fundamentally entwined with information about intensity because the spectrum of natural light is highly correlated (1–3). Accordingly, wavelength information must be extracted by comparing the signals from at least two spectrally distinct photoreceptors, in a process generally referred to as “colour opponency” (4). To this end, most animal eyes use up to five spectral types of photoreceptors for daylight vision, with around four being the norm for vertebrates (reviewed in (4)). However, our knowledge of how the signals from four or more spectral types of photoreceptors are harnessed at a circuit level to extract this specific chromatic information remains limited.

68

Increasing the diversity of available spectral photoreceptors exponentially expands the diversity of theoretically detectable spectral contrasts. However, there is a law of diminishing returns: In natural scenes, some spectral contrasts are much more abundant than others. For efficient coding (5–7), animal visual systems should therefore prioritise the specific contrasts that are particularly prevalent in their natural visual world.

69

70

71

72

73

74

Here, we explored how zebrafish extract wavelength and intensity information from their natural visual world. Like many surface-dwelling fish, already their larvae use the ‘full’ ancient tetrachromatic cone-photoreceptor complement comprising red-, green-, blue- and UV-cones (8). Importantly, their retinal circuits can be non-invasively monitored and manipulated in the live animal (9) to provide insights into the computation of colour in the intact circuit.

75

76

77

78

79

80

81

We asked three questions: (i) What is the *in vivo* spectral tuning of zebrafish cone-outputs at the synapse, (ii) what is the circuit implementation, and (iii) how does this specific tuning support efficient sampling and decomposition of natural light?

82

83

84

85

Surprisingly, we found that two of the four cone types (green and blue) are strongly opponent, while the remaining two (red and UV) are essentially non-opponent, despite feeding into the same horizontal cell network. We go on to show how this spectral tuning is anatomically and functionally implemented at the circuit-level using horizontal cells. Further, comparison of the spectral tuning of the four cone-types to the spectral statistics of natural light showed that this specific cone-tuning arrangement allows zebrafish to effectively ‘solve’ a major fraction of the basic wavelength discrimination problem already at the first synapse of their visual system: Red-cones encode “colour-invariant” achromatic information, green-cones encode “brightness-invariant” spectral information, blue-cones provide a second chromatic axis that can be further optimised by possible opposition to green cones downstream, while UV-cones by themselves provide a secondary ‘UV-achromatic’ signal – presumably for visual prey capture (10). These findings also strongly imply that ancestral vertebrate circuits for colour vision are built upon the opponent signals from green- and blue-cones, which are lost in mammals including in humans (4).

86

87

88

89

90

91

92

93

94

95

96

97

98

99

100

101

102 Finally, zebrafish are not alone in using such an efficient strategy. By
103 linking the spectral tuning of *Drosophila melanogaster* photoreceptors (11)
104 with hyperspectral natural imaging data (12) we note that fruit flies use
105 essentially the same strategy. However, their spectral tunings are
106 systematically blue-shifted compared to those of zebrafish, presumably to
107 directly acknowledge the relatively blue-shifted statistics of natural light in
108 air (13). Taken together, our findings highlight a potentially general circuit-
109 level mechanism of vision whereby incoming light is decomposed into
110 “colour” and “greyscale” components at the earliest possible site.

111

112

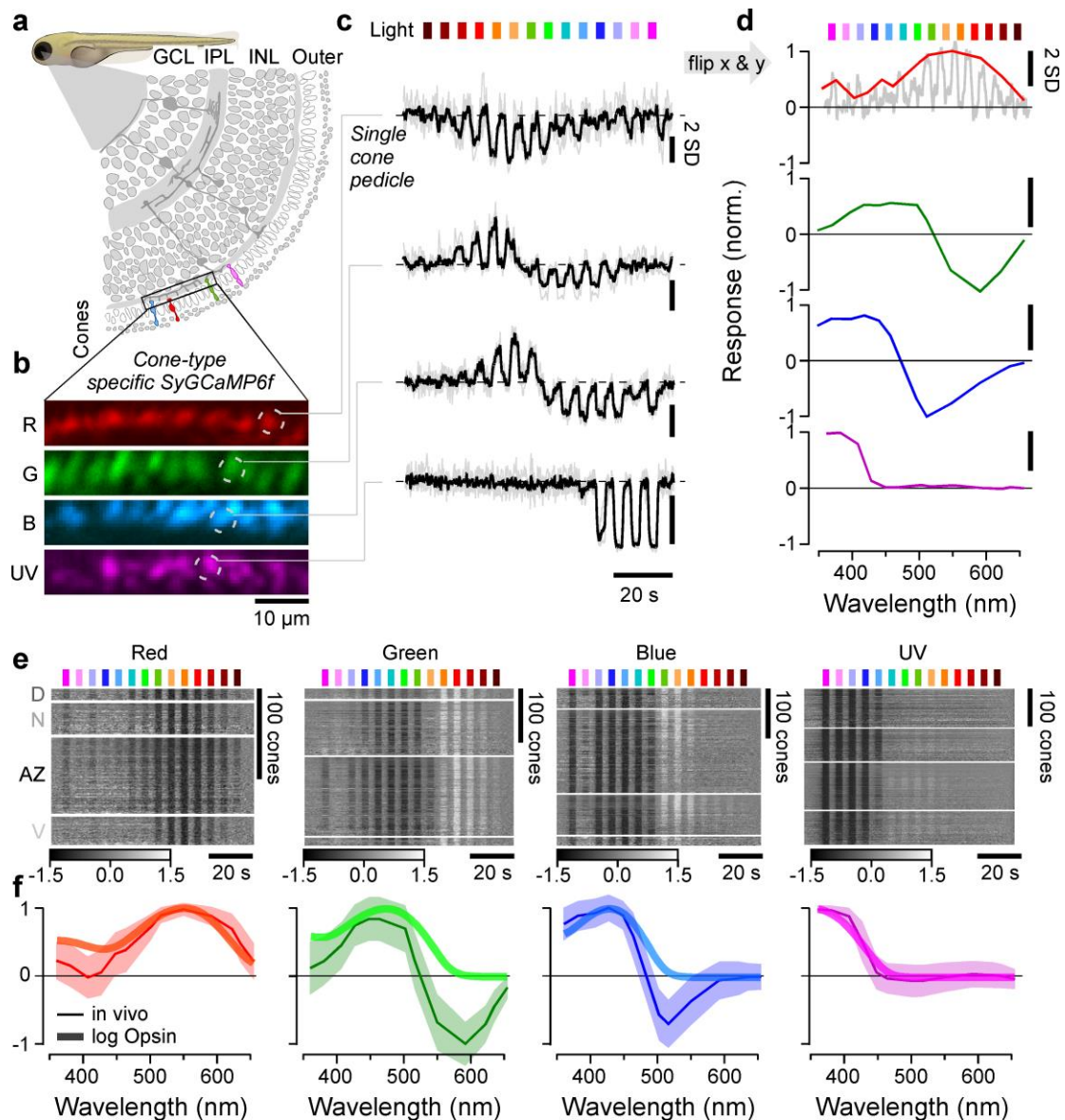
RESULTS

113 **Spectral tuning of zebrafish cones *in vivo*.** To determine spectral tuning
114 functions of the larval zebrafish’s four cone types (8) (red, green, blue, UV),
115 we custom-built a hyperspectral full-field stimulator based on an earlier
116 design (14) (Fig. S1a,b). A diffraction grating was used to reflect the light
117 from 14 LEDs (peaks: 360 to 655 nm) into a collimated fibreoptic that was
118 pointed at the live zebrafish’s eye mounted under a 2-photon (2P)
119 microscope. To avoid spectral cross-talk with the 2P imaging system, we
120 line-synchronised each LED’s activity with the scanner retrace (15, 16).
121 Together, this arrangement permitted spectrally oversampling the much
122 broader cone opsins (Fig. S1b,c) during *in vivo* 2P imaging in the eye. All
123 stimuli were presented as wide-field flashes from dark.

124 **Green and blue cones, but not red and UV cones, display strong**
125 **spectral opponency.** We generated four cone-type specific SyGCaMP6f
126 lines (Fig. 1a,b) (17) and measured the spectral tuning of each cone type
127 at the level of their pre-synaptic terminals (pedicles), i.e. their output (Fig.
128 1c,d). Here, cones connect with other cones via gap junctions (18), with
129 horizontal cells (HCs) which provide both feedback and feedforward
130 inhibition (19), as well as with bipolar cells (BCs) which carry the
131 photoreceptor signal to the feature extracting circuits of the inner retina
132 (20). We did not study rods, as these are functionally immature in zebrafish
133 larvae (21, 22).

134 From fluorescence traces, we extracted tuning functions (Methods),
135 inverting both the x- and y-axes (Fig. 1d and inset). The inversions were
136 done to display tuning functions from short- to long-wavelengths as is
137 conventional, and to compensate for the fact that vertebrate
138 photoreceptors hyperpolarise in response to light (23). We adhered to the
139 time-inversion henceforth to facilitate comparison between raw data and
140 summary plots (e.g. Fig. 1e). We systematically measured such tuning
141 functions for n = 409, 394, 425, 431 individual red-, green-, blue- and UV-
142 cones, respectively (n= 9, 11, 12, 7 fish). A total of n = 172, 288, 312, 410
143 recordings, respectively, passed a quality criterion (Methods, Fig. S1d-g)
144 and were kept for further analysis.

145



146

147

148

149

150

151

152

153

154

155

156

Figure 1 | In vivo spectral tuning of larval zebrafish cones and HC block. *a*, Schematic of larva zebrafish retina, with position of cone-pedicles highlighted (adapted from (75)). *b,c*, example scans of the four spectral cones (*b*, Methods) with single pedicle response examples for each (*c*) to 3 s flashes of light from each of the 14 LEDs (see Fig. S1a-c). Shown are the means superimposed on individual repeats. *d*, Example spectral responses summarised from (*c*) – note that in this representation, both the X and y axes are flipped relative to the raw responses. *e,f*, Population responses of each cone types recorded in different parts of the eye (D, Dorsal; N, Nasal; AZ, Acute Zone; V, Ventral – see also Fig. S1g) (*e*) and population mean $\pm 95\%$ confidence intervals with log-transformed respective opsin template superimposed (*f*, Methods). Heatmaps (*e*) are time-inverted to facilitate comparison to summary plots (*f*), greyscale bars are in z-scores.

157

158

159

160

161

162

163

164

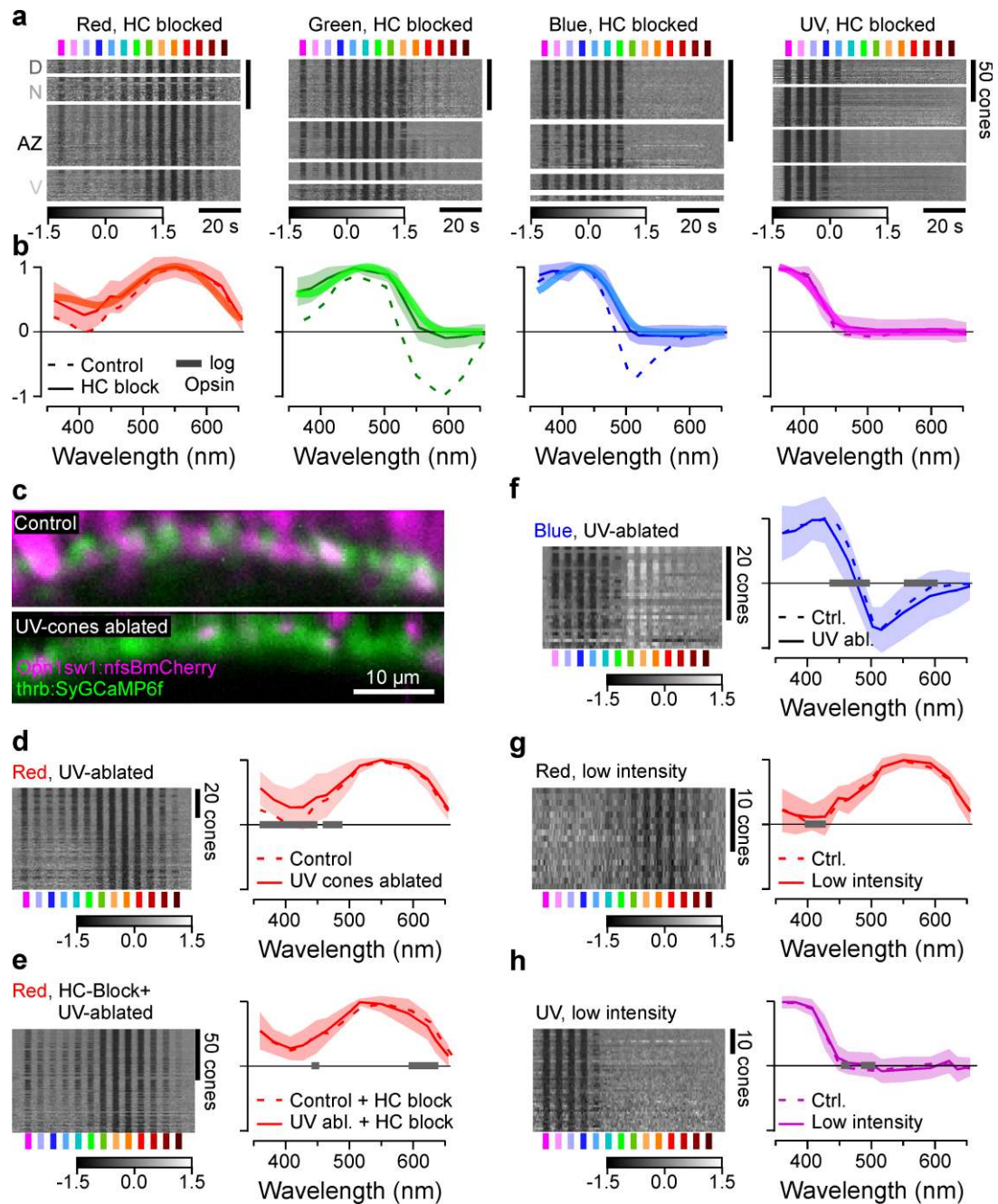
Because the larval zebrafish eye is both structurally and functionally asymmetrical (10, 13, 24–27), we always sampled from four different regions of the eye’s sagittal plane: dorsal (D), nasal (N), ventral (V) and the *area temporalis* (acute zone, AZ (also known as “strike zone” (13))). With exceptions noted below (see also Discussion), we found that the spectral tuning of cones was approximately eye-position invariant (Fig. S1g). For further analysis we therefore averaged across cones irrespective their position in the eye (Fig. 1e,f).

165 On average, red- and UV-cones had approximately monophasic (non-
166 opponent) output tuning functions that were largely in line with the tuning
167 function of their respective log-transformed opsins (Methods). Such a log-
168 transform is expected from the nature of signal transfer between outer
169 segment phototransduction to synaptic calcium in the pedicle (11, 28, 29).
170 Red-cones were broadly tuned and never exhibited opponency (Fig. 1f,
171 left). In fact, some individual red-cones hyperpolarised in response to all
172 tested wavelengths (Fig. 1e, left, cf. Fig. S1g). Nevertheless, on average
173 red-cone sensitivity was weakly suppressed in the UV-range compared to
174 the log-transformed opsin template (Discussion). In contrast, all UV-cones
175 were narrowly tuned up to the short-wavelength cut-off imposed by the eye
176 optics (~350 nm, unpublished observations). Their tuning curve near
177 perfectly matched the respective opsin template (Fig. 2f, right). UV-cones
178 in the AZ and ventral retina moreover exhibited weak but significant
179 opponency to mid-wavelengths (Fig. S1g, Discussion).

180 Unlike red- and UV-cones, the *in vivo* output tuning functions of green- and
181 blue-cones did not match their log-transformed opsin templates. Instead,
182 these cones consistently exhibited strong spectral opponency to mid-
183 and/or long-wavelength light (Fig. 1e,f, middle). Here, blue-cones had a
184 highly consistent zero-crossing at 483 ± 1 nm, while most green cones
185 inverted at 523 ± 1 nm (mean, 95% confidence intervals, Methods). Green-
186 cones in the acute zone were slightly long-wavelength shifted with a zero-
187 crossing at 533 ± 1 nm (Fig. S1g, Discussion).

188 Together, to our knowledge this establishes the first direct and *in vivo*
189 measurements of cone-pedicles' spectral tuning functions in a vertebrate.

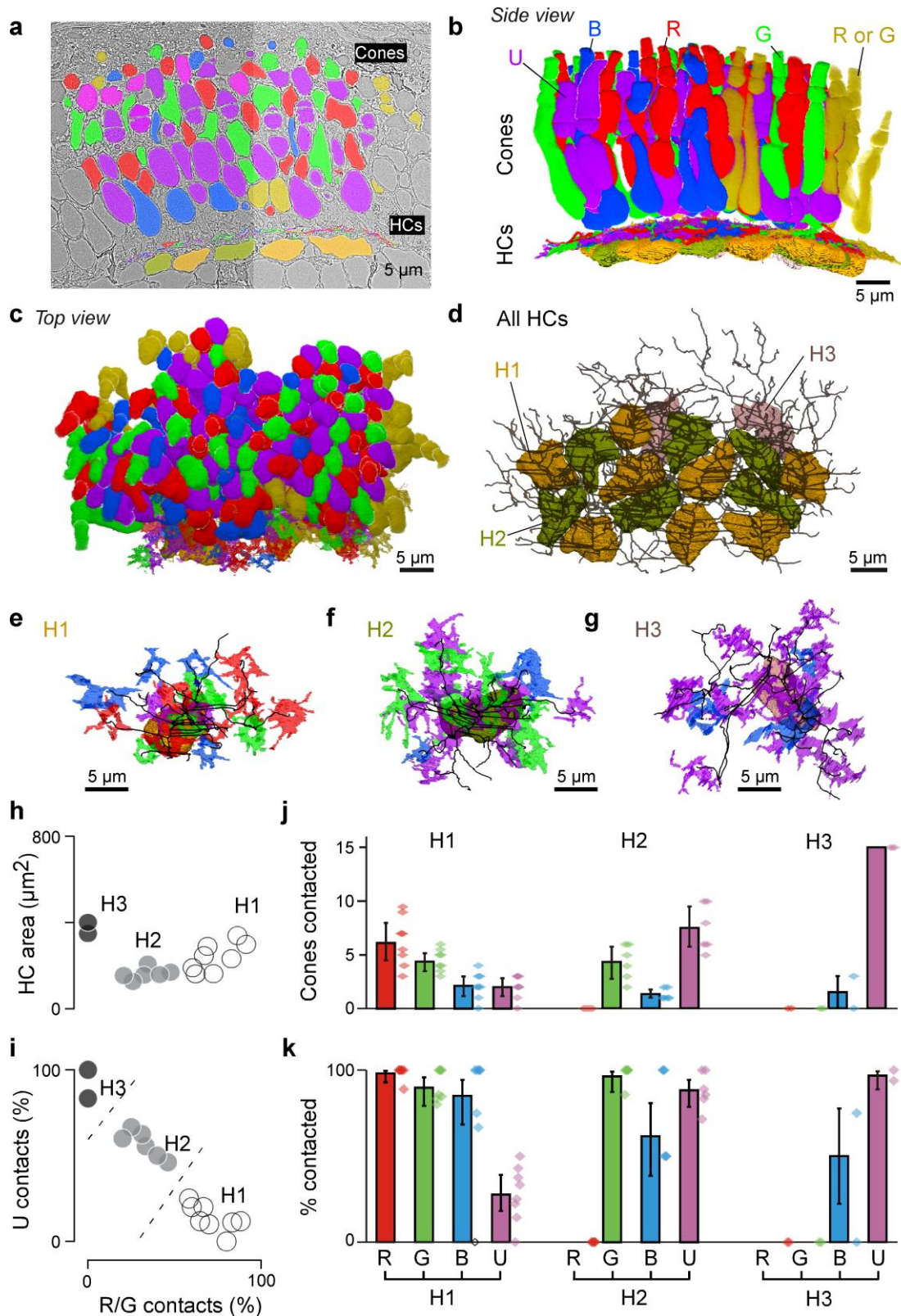
190 **Spectral tuning of zebrafish cones is fully accounted for by**
191 **expressed opsins and horizontal cell feedback.** The nature of
192 phototransduction in cone-photoreceptors dictates that the absorption of
193 photons leads to a drop in synaptic calcium. Accordingly, light-driven
194 increases in synaptic calcium (Fig. 1f) must come from a sign-inverting
195 connection from other cones, most likely via horizontal cells (HCs) (30, 31).
196 We therefore decoupled HCs by pharmacologically blocking the glutamate
197 output from cones using CNQX (Methods, Fig. 2a,b). This completely
198 abolished all spectral opponency and increased the UV-response
199 amplitude of red cones. As a result, now all four cone-tuning functions
200 were fully accounted for by the respective log-transformed opsins (Fig.
201 2a,b, Fig. S2a). Our results further implied that possible heterotypical cone-
202 cone gap junctions, if present, do not strongly contribute to spectral cone-
203 tuning. In support, cone-tunings were essentially invariant to additional
204 genetic ablation of UV-cones in the absence of HCs (Fig. 2c-f). Moreover,
205 reducing overall stimulus brightness to probe for possible response
206 saturation had no major effects on tuning functions (Fig. 2g,h). Taken
207 together, our results strongly suggest that *in vivo*, the spectral tuning of all
208 zebrafish cones is driven by the expressed opsin variant and shaped only
209 by specific connections with HCs relaying feedforward signals from other
210 cones. What are these HC connections?



211

212 **Figure 2 | Opsin-like cone-responses in the absence of horizontal cells. a,b**, Population
 213 responses of each cone type during pharmacological blockage of HCs (a, Methods) and population
 214 mean \pm 95% confidence intervals with log-transformed respective opsin template superimposed (b,
 215 Methods). **c**, pharmacogenetic UV-cone ablation in the background of red-cone GCaMP labelling
 216 before (top) and 24h after 2h treatment of metronidazole (10 mM) application (bottom, Methods). **d**,
 217 red-cone tunings after UV-cone ablation ($n = 77$) (d) and after additional pharmacological HC
 218 blockage ($n = 103$) (e). Shown are heatmaps (left) and means \pm SD (solid lines+shadings), and
 219 analogous data in the presence of UV-cones (dotted, from Figs. 1f, 2b). Note that the 361 nm LED
 220 was omitted in this experiment. **f**, as (d), but here recording from blue cones ($n = 30$). **g,h**, red- ($n =$
 221 17) (g) and UV-cone tunings ($n = 43$) (h) at \sim 9-fold reduced overall stimulus-light intensities (solid
 222 lines + shadings, Methods), compared to tunings at 'standard' light intensities (from Fig. 1f). Grey
 223 bars on the x-axis in (d-h) indicate significant differences based on the 99% confidence intervals of
 224 the fitted GAMs (Methods). Note that heatmaps (a,d-h) are time-inverted to facilitate comparison to
 225 summary plots (b, d-h). Grey-scale bars in z-scores.

226



227

228 **Figure 3 | Connectomic reconstruction of outer retinal circuitry.** **a**, Example vertical electron microscopy
 229 (EM) section through the outer retina, with cones and horizontal cells painted. Cones are colour coded by their
 230 spectral identity, with “yellow cones” indicating red- or green-cones at the section edge that could not be
 231 unequivocally attributed (Methods); HCs: H1, yellow/brown; H2, dark green, H3: light pink. **b-d**, Full volumetric
 232 reconstruction of all cones and skeletonised HCs in this patch of retina, shown from the side (**b**), top (**c**) and HC’s
 233 only (**d**). **e-g**, example individual HCs classified as H1 (**e**), H2 (**f**) and H3 (**g**) with connecting cone pedicles. **h-k**,
 234 Quantification of HC dendritic area (**h**, cf. Fig. S3g) and cone contacts (**j-k**) shown as absolute numbers with
 235 bootstrapped 95% CI (**j**) and percentage of cones in dendritic territory with binomial CI (**i,k**).

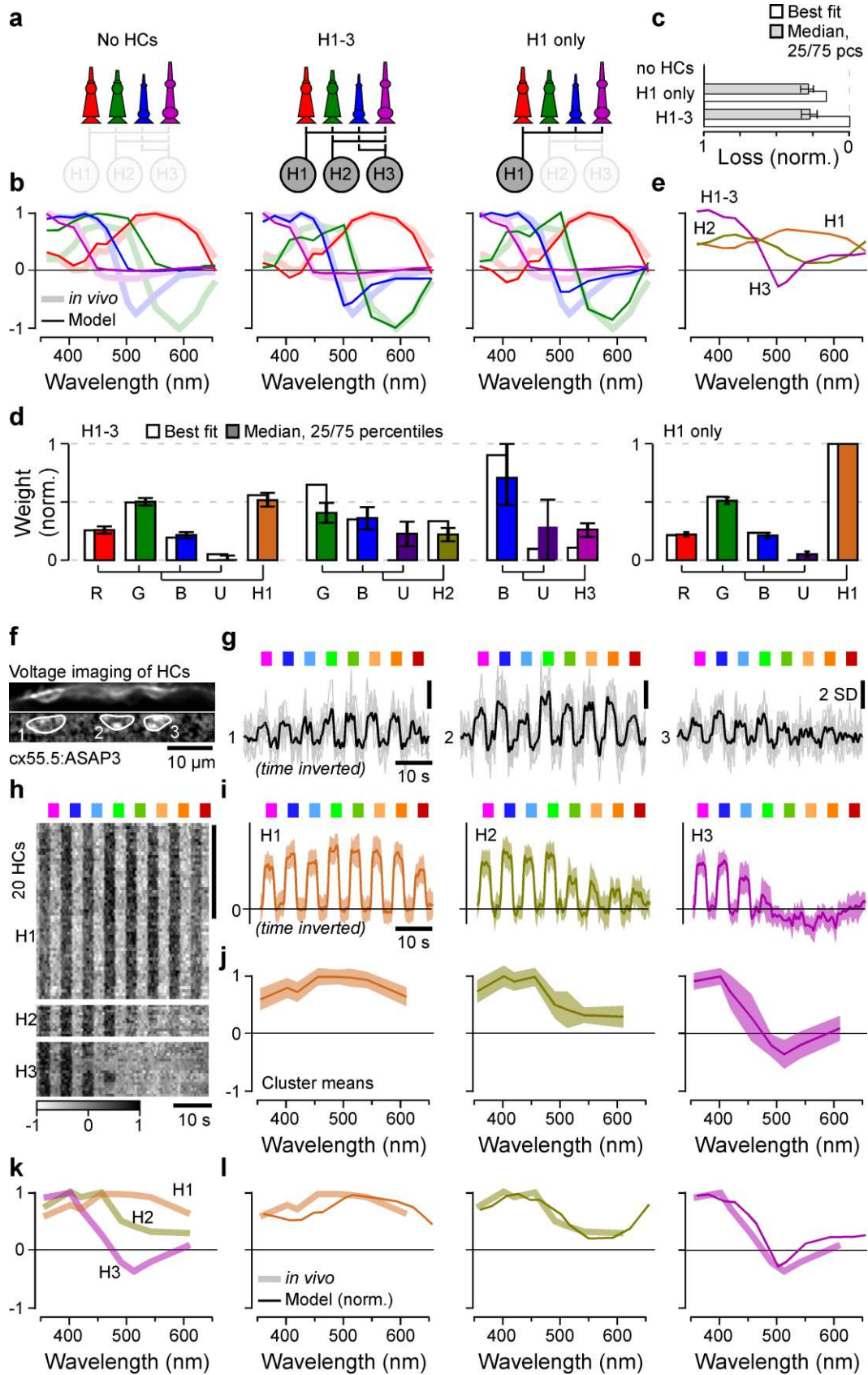
236 **A connectome of the larval zebrafish outer retina.** Light-microscopy
237 studies in adult zebrafish have described at least three types of cone-HCs
238 (H1-3), which contact R/G/B/(U), G/B/U and B/U cones, respectively (30,
239 32). However, for larval zebrafish HC-types and their connections to cones
240 are not known except for H3 (33). To complete this gap in knowledge we
241 used a connectomics approach based a combination of serial-section
242 electron microscopy (Fig. 3) and confocal imaging (Fig. S3, Methods). In
243 total, we reconstructed a 70 x 35 x 35 μm patch of larval outer retina in the
244 acute zone, which comprised $n = 140$ cones $n = 16$ HCs (Fig. 3a-d). UV-
245 and blue-cones were identified directly in the EM-volume based on their
246 characteristic OPL-proximal mitochondrial pockets (UV, Fig. S3a) and
247 somata (blue, Fig. S3b), respectively. This allowed initially sorting cones
248 into three groups: UV, blue and red/green. Next, we traced each HC's
249 dendritic tree and identified their connections to cones belonging to each of
250 these cone-groups (Fig. 3d-k, Fig. S3c-h). Relating each HC's relative
251 connectivity to UV-cones to their connections to red/green-cones allowed
252 separating HCs into three groups (Fig. 3i, Fig. S3g), which were verified by
253 clustering the HCs on all extracted features (Methods). These were dubbed
254 H1, H2, and H3, based on their similarity to known adult HC types (32, 34,
255 35). The same classification was then further confirmed by confocal
256 microscopy (Fig. S3d-h). Of these, H1 reliably contacted all red/green-
257 cones within their dendritic field, while H2 systematically avoided
258 approximately half of these cones. In line with confocal data (Fig. S3), this
259 allowed disambiguating red-cones (contacted only by H1) from green-
260 cones (contacted by both H1 and H2). With the exception of $n = 14$ of 66
261 red-green cones that could not be unequivocally allocated due to their
262 location at the edge of the volume (yellow, counted as 0.5 red, 0.5 green in
263 Fig. 3b,d), this completed cone-type identifications.

264 From here, we quantified each HC groups' connections to the four cone
265 types. This revealed that H1 contacted essentially all red-, green- and blue-
266 cones within their dendritic fields, but imperfectly avoided UV-cones (Fig.
267 3j,k). In contrast, H2 by definition never contacted red-cones, but contacted
268 all other cones including UV cones. Finally, H3 was strongly dominated by
269 UV-cone contacts, with a small contribution from blue-cones. H3 never
270 contacted red- or green-cones. Together, this largely confirmed that adult
271 HC connectivity is already present in larvae, and moreover contributed
272 cone-weighting information for the three HC types. We next asked how this
273 specific HC-connectivity matrix underpins cone-spectral tunings.

274 **H1 horizontal cells likely underlie most spectral tuning.** To explore how
275 the three HC-types contribute to spectral cones-tunings, we first set up a
276 series of functional circuit models for all possible combinations of HCs
277 (Methods). These linear models included the established connectivity
278 structure (Fig. 3k) and were driven by the cone tunings in the absence of
279 HCs (Fig. 2a), with the goal of explaining cone-tunings in the presence of
280 HCs (Fig. 1f). We computed posteriors for the model parameters using
281 likelihood-free inference (36) based on the cones' tunings, and we

282
283

assumed sign-preserving connections from cones to HCs but sign-inverting connections from HCs to cones.



284

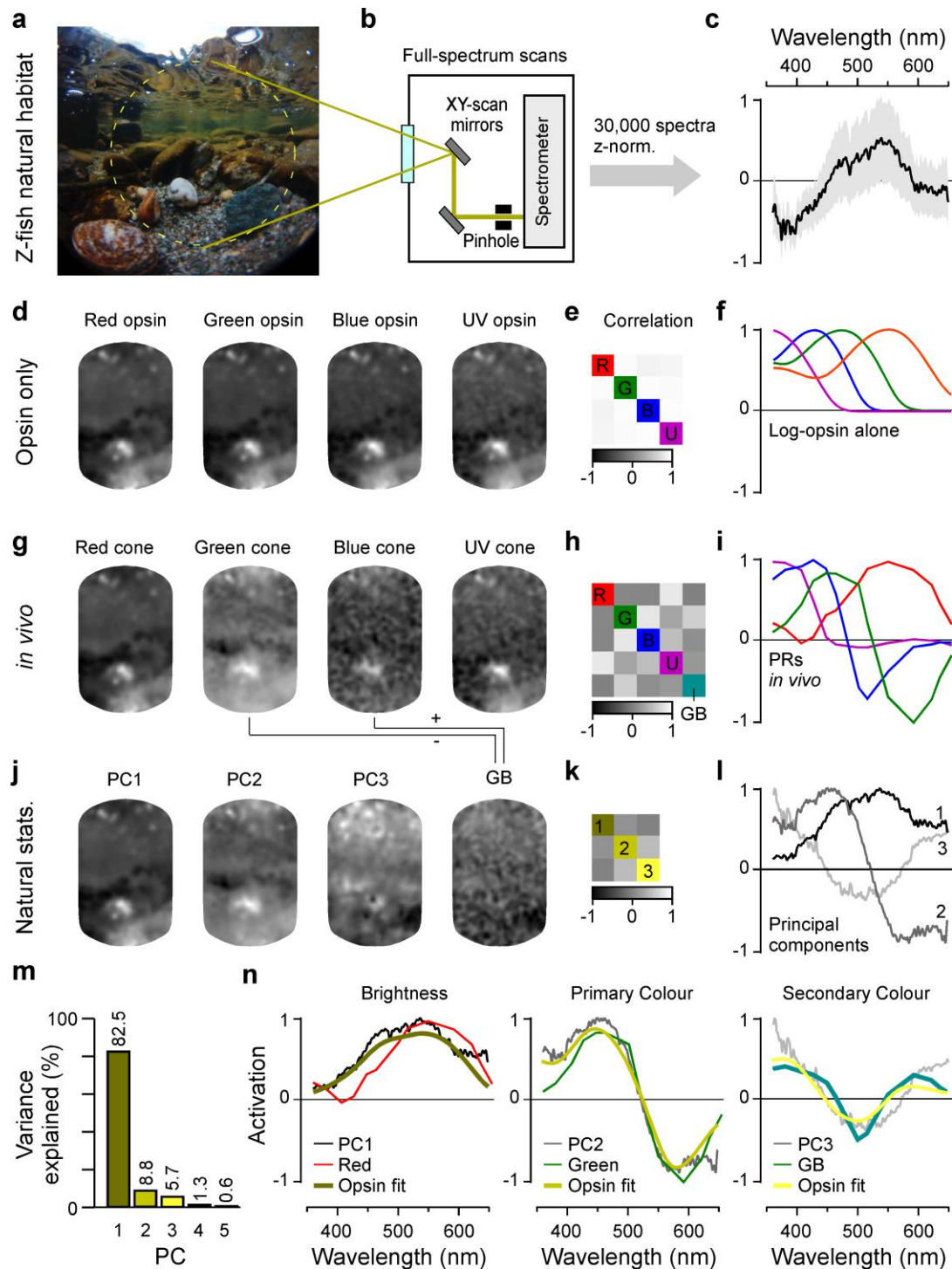
285 **Figure 4 | Spectral tuning of cones by horizontal cells. a-e**, linear model of spectral tuning in an outer retinal
286 network comprised of 4 cone- and 3 HC-types, with maximum connectivity matrix defined as in Fig. 3k (Methods).
287 Cone tunings are initiated based on *in vivo* data during HC block (Fig. 2b). Different HC combinations include (a,
288 from left): no HCs, all HCs and H1 only. In each case, the model computes resultant cone-tunings (solid lines)
289 superimposed on *in-vivo* data in the absence of HC block (shadings, from Fig. 1f) (b), reconstruction quality (c) as
290 loss relative to the peak performance for the full H1-3 model (loss = 0) and in the absence of HCs (loss = 1) and
291 normalised weights such that cones contributing to a given HC, and HCs contributing to the full model, each add
292 up to 1 (d). In addition, resultant HC tunings are shown for the full H1-3 model (e). **f-j**, *in vivo* voltage imaging of
293 HC somata's spectral tuning (Methods). **f,g** example scan (f, average image (top) and local response correlation
294 (76) and ROIs (bottom)) and responses (g, mean superimposed on individual repeats). **h-j**, results of clustering of
295 mean responses from $n = 86$ ROIs (h, $n = 15$ fish) with cluster means (i) and extracted tuning functions (j,
296 means \pm SD). **k,l**, mean tunings of *in vivo* HC clusters (k, from j), and superposition of each measured modelled
297 (solid lines, from e) and measured (shading, from k) HCs. Note that raw- (g) and averaged (i) HC-responses as
298 well as the summary heatmap (h) are time-inverted to facilitate comparison with summary plots (j-l). Greyscale
299 bar in (h) in z-scores.

300 The model recapitulated well the *in-vivo* tuning functions of all cones when
301 simultaneously drawing on all three HC types. However, almost the same
302 fit quality was achieved when using H1 alone (Fig. 4a-d, cf. Fig. S4a-c),
303 while H2 mainly fine-tuned the blue- and UV-cones and H3 had negligible
304 impact on any cone-tunings (Fig. S4a). In fact, any model that included H1
305 outperformed any model that excluded H1 (Fig. S4a-c). H1, where present,
306 also consistently provided the strongest feedback amongst HCs (Fig. 4d,
307 Fig. S4c). Together, modelling therefore suggests that H1-like HCs are the
308 main circuit element underlying the *in-vivo* spectral tuning of zebrafish
309 cones. Moreover, the inferred relative cone-type weighting for H1
310 approximated their anatomical connectivity established by EM (Fig. 4j),
311 with the exception of green-cones which had stronger-than-expected
312 weights (Fig. 4d) – possibly uncovering an increased synaptic gain at this
313 site.

314 Next, we sought to verify the model by experimentally measuring the
315 spectral tunings of HCs and comparing these to the predicted HC tunings
316 from the full model (Fig. 4e). For this, we used *in vivo* 2P voltage imaging
317 of HCs somata using ASAP3 (37) (Fig. 4f-l) (Methods). In total, recordings
318 from $n = 86$ HCs that passed a quality criterion (Methods) were sorted into
319 three clusters (Methods). The largest cluster exhibited a spectrally broad,
320 monophasic response that closely matched the model's prediction for H1
321 (Fig. 4l, see also (30, 34)). Next, short-wavelength biased clusters 2 and 3
322 closely matched the model's prediction for H2 and H3, respectively (30,
323 34).

324 **Efficient encoding of achromatic and chromatic contrasts in natural**
325 **light.** To explore how the specific *in vivo* cone tuning functions may
326 support zebrafish vision in nature, we next computed the distribution of
327 achromatic and chromatic content of light in their natural habitat. For this,
328 we used a total of $n = 30$ underwater hyperspectral images (1,000 pixels
329 each: 30,000 spectra) (12, 13) (Fig. 5a-c). Using one example scan for
330 illustration (Fig. 5a), we first computed each cone's view of the world in the
331 absence of outer retinal feedback by taking the dot product of each log-
332 transformed opsin spectrum with each pixel spectrum (Fig. 5d-f).

333



334

335 **Figure 5 | In vivo cone tunings efficiently represent statistics of natural light.** **a-c**, Hyperspectral data
 336 acquisition from zebrafish natural visual world. A 60° window around the visual horizon of an example scene
 337 recorded in the zebrafish natural habitat (a) was sampled at 1,000 equi-spaced points with a custom-built
 338 spectrometer-based scanner (b) to yield 1,000 individual spectral readings from that scene. (c) summarises
 339 the pooled and z-normalised data from $n = 30$ scenes (30,000 spectra) with $\text{mean} \pm \text{SD}$ (data from (13)). **d-l**,
 340 reconstructions and analysis of the example scene as see through different spectral filters: (d-f) log-opsin
 341 spectra, (g-i) cone *in vivo* tunings and (j-l) based on first three principal components (PCs) that emerge from the
 342 hyperspectral data shown in (c). From left to right: (d,g,j) example scene (from a) reconstructed based on opsin-
 343 *in vivo*-/PC-tunings as indicated, (e,h,k) correlation matrices between these respective reconstructions and (f,i,l)
 344 the actual tunings/PCs. A 5th element “GB” (for “green/blue”) is computed for *in vivo* tunings as contrast between
 345 green- and blue-cone tunings (cf. Fig. S5). **m**, % variance explained by the first five principal components (l). **n**,
 346 Superposition of cone *in vivo* tunings (coloured lines), PCs, and a linear R/G/B/U log-opsin fit to the respective
 347 PC (yellows, Methods). The latter fit can be seen as the biologically plausible optimum match to a given PC that
 348 can be achieved in a linear regime.

349 In this configuration, the intensity-normalised representations of the scene
350 by each of the four cones were extremely similar as expected from high
351 spectral correlations in natural light (Fig. 5d). In contrast, when the same
352 scene was computed for the intact outer retinal network by taking the *in*
353 *vivo* cone-tuning functions (from Fig. 1f), the different cones instead
354 delivered much more distinct images (Fig. 5g-i).

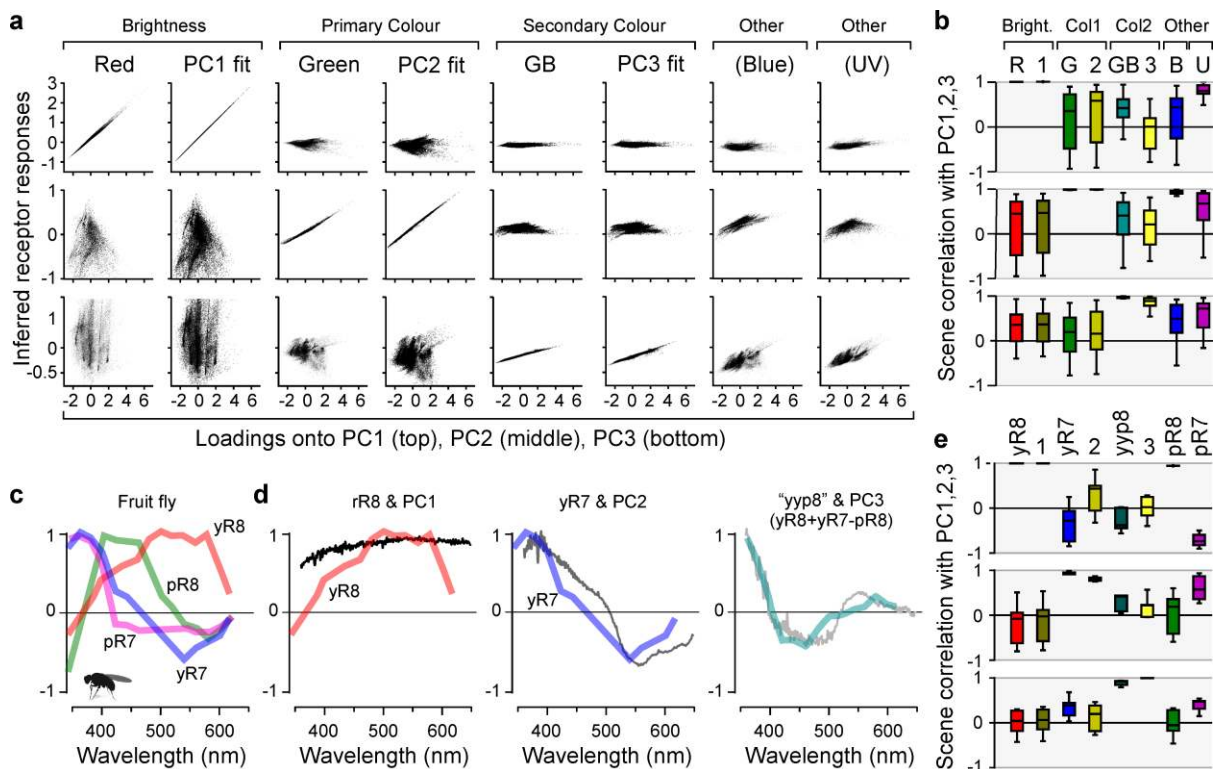
355 Next, to determine the spectral axes that optimally captured the variance of
356 natural light in the zebrafish's natural underwater world (Discussion), we
357 used principal component analysis (PCA) across the spectra of all $n =$
358 30,000 pixels in the data set (Fig. 5c, j-l). Due to the strong spectral
359 correlations in natural light, the first component (PC1) captured the
360 achromatic ("black and white") image content, while subsequent
361 components (PC2, PC3 etc.) captured the major chromatic ("colour") axes
362 in decreasing order of importance (1, 5). Together, PCs 1-3 accounted for
363 97% of the natural spectral variance (Fig. 5m). We computed what the
364 example scene would look like if sampled by detectors that were directly
365 based on the first three principal components. We found that scenes
366 processed by PC1 and PC2 (Fig. 5j) were highly reminiscent of the scenes
367 sampled by *in vivo* red- and green cones, respectively (Fig. 5g). Next, PC3
368 was not obviously captured by either of the remaining blue- or UV-cones in
369 isolation, however it did approximately resemble the scene when
370 reconstructed by a green/blue-cone opponent axis ("GB", turquoise,
371 Discussion). In fact, PC3 could be approximated by a variety of cone-
372 combinations, however all best-matches ($\rho=0.97$, Methods) required
373 opposing green- and blue-cones (Fig. S5).

374 Direct superposition of these cone-output spectra with the respective
375 principal components further illustrated their striking match (Fig. 5n). These
376 cone-spectra were also well matched by a direct fit to the principal
377 components when using the four cones' opsin-templates as inputs (Fig. 5n,
378 yellows, Methods). Here, our rationale was that these opsin-fits present a
379 biologically plausible optimum for mimicking the principal components.

380 To quantitatively explore this match and its consequences for the encoding
381 of natural light, we next computed how each of the 30,000 individual
382 collected spectra would activate red- and green-cones as well as the GB-
383 axis. We then plotted these activations against the respective loadings of
384 PC1-3 for these spectra (Fig. 6a). In each case, we also computed the
385 same metric for the best log-opsin fits to the PCs. This confirmed the
386 excellent performance of the system for separating achromatic from
387 chromatic information under natural light. Red-cone activation correlated
388 almost perfectly (mean $\rho>0.99$, 2.5/97.5 percentiles 0.99/ >0.99) with
389 spectral loadings against PC1 (Fig. 6a, top left, cf. Fig. 6b, top left), but was
390 uncorrelated with either PC2 ($\rho=-0.16$, -0.89/0.88) or PC3 ($\rho=0.29$, -
391 0.34/0.91) (Figs. 6a,b, middle and bottom left). Moreover, red-cone
392 performance was near-indistinguishable from that of the opsin fit against
393 PC1 ($\rho>0.99$, $>0.99/>0.99$), which was used as a biologically plausible
394 benchmark of optimality (Figs. 6a,b, second column). Accordingly, and

395
396
397
398
399
400
401
402
403
404
405

despite the minor differences in short-wavelength activation of the red-cone action spectrum compared to PC1 and its opsin fit (Fig. 5n, left, Discussion), red-cones encoded natural achromatic contrast (i.e. “brightness”, PC1) with negligible contamination of chromatic information (i.e. PCs 2,3). In contrast, activation of green-cones was highly correlated with PC2 ($\rho=0.99$, $0.98/>0.99$), but uncorrelated with either PC1 ($\rho=-0.15$; $-0.88/0.88$) or PC3 ($\rho=0.14$, $-0.66/0.81$, Figs. 6a,b columns 3). Again, their performance was near-indistinguishable from that of the respective opsin fit (Figs. 6a,b, columns 4). Accordingly, green-cone activation carried no information about brightness, but instead encoded an efficient primary chromatic signal.



406

407 **Figure 6 | Encoding of natural achromatic and chromatic contrast.** **a**, Computed “responses” of *in vivo*
408 cones, the GB-axis, and each respective log-opsin PC-fit (all from Fig. 5i,n) to each of the $n = 30,000$ individual
409 natural spectra, plotted against (each spectrum’s loadings onto PC1 (top row), PC2 (middle row) and PC3
410 (bottom row), as indicated. “Responses” plotted on y-axes, PC-loadings on x-axis. In general, a column that
411 shows a near-perfect correlation in one row, but no correlation in both other rows (e.g. column 1) can be seen as
412 a tuning function that efficiently captures the respective PC (e.g. column 1 shows that red-cones efficiently
413 represent PC1 but not PC2 or PC3). **b**, Corresponding summary statistics from (a), based on scene-wise
414 Spearman-correlations. **c**, Spectral tuning functions of *Drosophila* R7/8 photoreceptors as measured *in vivo* at
415 their synaptic output (data from (11)). **d**, comparison of *Drosophila* tuning functions with the first three PCs that
416 emerge from terrestrial natural scenes (data from (12)). Here, PC3 is matched with a “yyp8” axis as indicated (cf.
417 Fig. S6d-f). **e**, Summary stats of *Drosophila* photoreceptor “responses” to each of the $n = 4,000$ individual
418 terrestrial natural spectra plotted against their respective PC loadings.

419
420
421
422
423
424
425

Next, both activation of the GB-opponent axis and of the corresponding opsin fit correlated strongly with PC3 ($\rho=0.95$, $0.80/0.99$; $\rho=0.79$, $0.18/0.99$, respectively), but not with PC1 ($\rho=0.38$, $-0.25/0.92$; $\rho=-0.08$, $-0.76/0.52$) or PC2 ($\rho=0.31$, $-0.62/0.91$, $\rho=-0.15$, $-0.80/0.57$, Figs. 6a,b, columns 5,6). Accordingly, contrasting the signals of blue- and green-cones offers the theoretical possibility to build an efficient secondary chromatic signal in downstream circuits (Discussion). Notably, blue-cones

426 in isolation correlated mainly with PC2 ($\rho=0.94$, 0.85/0.99) rather than PC1
427 ($\rho=0.18$, -0.74/0.91) or PC3 ($\rho=0.43$, -0.33/0.90) (Figs. 6a,b, columns 7),
428 suggesting that they could potentially serve to provide an alternative route
429 to encoding primary chromatic information.

430 Finally, UV-cones mainly correlated with PC1 ($\rho=0.80$, 0.51/0.99),
431 suggesting that this ultra-short-wavelength channel may serve to provide a
432 secondary achromatic signal (Figs. 6a,b, columns 8). However, its
433 performance in doing so was substantially inferior to that of red-cones,
434 suggesting that its primary function is not the encoding of achromatic
435 brightness *per se*, but rather to specifically detect short-wavelength signals.
436 Here, their weak but significant opponency to spectrally intermediate
437 signals may serve to accentuate contrast against an otherwise “grey”
438 background (Discussion).

439 Taken together, it appears that larval zebrafish effectively ‘rotate’ colour
440 space already at their visual system’s first synapse signal along an
441 achromatic axis (red-cones) and a primary chromatic axis (green-cones),
442 with the added possibility to build an efficient secondary chromatic axis by
443 opposing green- and blue-cones downstream. Together, this system
444 captures at least 91.3% of spectral variance in natural scenes when using
445 red- and green- cones alone, and potentially up to 97% if including green-
446 blue opponency. Elegantly, it also leaves UV-cones to serve independent
447 visual functions, such as prey capture of UV-bright microorganisms (10)
448 (Discussion).

449 **A comparison to spectral processing in fruit flies.** A conceptually
450 similar decomposition of natural light may also be used in *Drosophila*
451 *melanogaster* (Fig. 6c-e, Fig. S6), the only other tetrachromatic species
452 where *in vivo* spectral tuning functions of photoreceptor outputs are
453 available (11). In these flies, R1-6 photoreceptors express a mid-
454 wavelength sensitive opsin and are generally considered an achromatic
455 channel, while R7/8-type photoreceptors are associated with colour vision
456 (38). We therefore compared spectral tuning curves of the four varieties
457 (yR8, yR7, pR8, pR7) of *Drosophila* R7/8-type photoreceptors (Fig. 6c,
458 taken from (11)) with the principal components that emerged from natural
459 spectra of $n = 4$ daytime field and forest scenes (12), each comprising
460 1,000 individual spectra as before (Fig. 6d,e, Fig. S6a-g, Discussion).

461 Like for zebrafish, this showed that their spectral tuning curves were well
462 approximated by the first three terrestrial PCs: PC1 and yR8 ($\rho>0.99$,
463 0.99/ >0.99), PC2 and yR7 ($\rho=0.93$, 0.91/0.98) and finally PC3 by opposing
464 jointly opposing both yR8 and yR7 against pR8 (for simplicity: “yyp8”,
465 $\rho=0.72$, 0.60/0.84, Fig. 6d,e, cf. Fig. S6d-g). Compared to zebrafish, the
466 spectral matches between photoreceptor action spectra and natural PCs
467 were however slightly worse, which may in part be linked to the use of a
468 smaller natural imagery dataset, and to the comparatively lower spectral
469 resolution information currently available in flies. Nevertheless, this general
470 match was made possible by the fact that, in line with the relatively

471 increased predominance of short-wavelength light above the water (Fig.
472 S6a), all terrestrial principal components (Fig. S6b) and corresponding
473 action spectra (Fig. S6g) were blue-shifted relative to those of aquatic
474 environments and of zebrafish, respectively.

475 Together, this suggests that ‘rotating’ colour space into primary achromatic
476 and chromatic axes (i.e. PC1-2) as early as possible, while leaving the
477 ultra-short wavelength system largely isolated, may be a fundamental
478 principle of colour vision when using more than two spectrally well-
479 separated photoreceptor types, in a striking example of convergent
480 evolution (Discussion).

481

482 DISCUSSION

483 Our physiological recordings from cones (Figs. 1,2) and horizontal cells
484 (Fig. 4f-l), linked to synaptic level EM-reconstructions (Fig. 3) and
485 computational modelling (Fig. 4a-e) provide a comprehensive *in vivo*
486 account of spectral processing for an efficient decomposition of natural
487 light (Figs. 5,6) at the visual system’s first synapse in a tetrachromatic
488 vertebrate.

489 **Linking retinal colour opponency to the principal components of**
490 **natural light spectra.** Using PCA of light spectra for understanding the
491 encoding of natural scenes by animal visual systems has a long tradition,
492 for example in information-theoretic considerations by Buchsbaum and
493 Gottschalk in 1983 (1). This seminal work described how the three
494 primaries of the human eye (long- mid- and short-wavelength sensitive:
495 L/“red”, M/“green”, S/“blue”, respectively) can be efficiently combined to
496 derive one achromatic and two chromatic axes with none, one and two
497 zero crossings, respectively. These theoretically optimal channels
498 corresponded well to psychophysically determined opponent mechanisms
499 in human vision, and were later shown to capture much of the spectral
500 variance in natural light (3). However, in contrast to zebrafish, the circuit
501 mechanisms that enable this striking link between the human primaries and
502 perception involve multiple levels of computation across both the retina
503 and the brain remain incompletely understood: First, many retinal ganglion
504 cells (RGCs) and their central targets, including in visual cortices, are
505 mid/long-wavelength-biased and non-opponent, and encode achromatic
506 contrasts (39). Second, inherited from probably non-selective retinal wiring,
507 midget circuits carry “red-yellow” or “green-yellow” spectral information that
508 is thought to be decoded into a primary “red-green” colour-opponent axis in
509 the central brain by mechanisms that remain largely unsolved. Third, at
510 least three types of “blue-yellow” RGCs contrast the signals from blue-
511 cones against the sum of red- and green-cones. This RGC opponency is
512 mainly achieved at the level of RGC dendrites, by contrasting the signals of
513 approximately non-opponent inner retinal neurons (40).

514 In addition, primate blue-cones themselves are yellow-blue opponent due
515 to feed-forward inputs of red-/green-cone inputs via HCs (41) – reminiscent
516 of the strategies employed by zebrafish cones. However, primate blue- and
517 red-/green-cones are homologous to zebrafish UV- and red-cones,
518 respectively (42, 43), and the HC underlying is H2 (40). Accordingly,
519 spectral opponency in primate blue-cones is presumably linked to the weak
520 but significant mid-wavelength opponency of zebrafish UV-cones, rather
521 than the much stronger opponency of zebrafish green- or and blue-cones
522 (Fig. 1f).

523 Beyond primates, comparative circuit knowledge of vertebrate retinas for
524 spectral processing is sparse and mainly restricted to dichromatic
525 mammals (4). Amongst tetrachromats that retain ancestral green- and
526 blue-cones, measurements of spectral responses in adult HCs of diverse
527 species of fish (30, 34, 44) are in good agreement with our *in vivo* HC data
528 in larval zebrafish. Moreover, zebrafish inner retinal neurons (8, 13, 24, 45)
529 display both non-opponent as well as a wide diversity of opponent
530 responses that generally prioritise simple short-vs.-long wavelength
531 computations over more complex combinations, broadly in agreement with
532 predictions from theory (1). However, in the absence of systematic and
533 spectrally resolved sensitivity measurements of zebrafish inner retinal
534 neurons, it has not been possible to explicitly link their properties to the
535 variance in natural visual light. In addition, direct *in vivo* spectral
536 measurements of zebrafish cone-photoreceptor outputs have remained
537 outstanding.

538 Amongst invertebrates, *Drosophila melanogaster* stands out as the only
539 tetrachromatic species where spectrally resolved photoreceptor output
540 tuning functions are available (11). As discussed, these reveal a
541 conceptual match to those of zebrafish, even down to circuit
542 implementation involving a single horizontal-cell-like feedback neuron - all
543 despite their eyes having evolved independently since long before the
544 emergence of image-forming vision in any animal. Here, the authors draw
545 on Buchsbaum and Gottschalk's ideas on efficient encoding (1) to suggest
546 that like for zebrafish bipolar cells (13), the *Drosophila* R7/8 single and
547 double zero-crossings can be conceptually matched with opsin-based
548 primary and secondary colour axes, respectively. However, how this link
549 would look like in practise for the encoding of spectral variance in natural
550 light remained unclear. Here, we extend these theoretical links to directly
551 show how like in zebrafish, *Drosophila* PC1 and PC2 are each well
552 captured by a single receptor, while capturing PC3 requires possible
553 opposing of multiple receptors downstream.

554 **Achromatic signalling.** Natural scenes are generally dominated by
555 achromatic over chromatic contrasts (5), and biased to mid- or long-
556 wavelengths. Accordingly, an efficient achromatic encoder should
557 approximate the resultant mid-/long-wavelength biased mean spectrum of
558 light in a non-opponent manner - as is the case for both zebrafish red-
559 cones (Fig. 2n) and for *Drosophila* yR8 photoreceptors (Fig. 6d). Here, the

560 quality of the spectral match primarily impacts the maximal achievable
561 signal-to-noise of the encoder, rather than its ability to encode brightness
562 *per se* (46, 47). Accordingly, despite their minor respective mismatches
563 compared to the mean of available light (see below), both zebrafish (Fig.
564 6a,b) and *Drosophila* implementations (Fig. 6d,e) capture PC1 well. For the
565 same reason, also other non-opponent photoreceptors, such as *Drosophila*
566 R1-6 (48) as well as vertebrate rods or “true” double-cones in many non-
567 mammalian vertebrates, are generally thought to capture achromatic
568 signals (4). However, in all these cases the presumed non-opponent
569 nature at the level of their synaptic output *in vivo* remains to be confirmed.

570 In both zebrafish red-cones, and in *Drosophila* yR8, the largest mismatch
571 to their natural environment’s PC1 was in the UV-range (Figs. 2n, 6d).
572 Here, it is tempting to speculate that their low short-wavelength sensitivity
573 is linked to a need to isolate behaviourally critical “general” achromatic
574 signals from those that incur specifically in the UV-range. In the case of
575 zebrafish, UV-specific signals carry key visuo-ecological relevance, in that
576 they can report the presence of prey (10) – a rare feature that is unlikely to
577 be captured in our scene-wide data of natural spectra (see also discussion
578 on UV-signalling below).

579 Ultimately, the signals from red-cones must be read out by downstream
580 circuits, in a manner that approximately preserves their spectral tuning.
581 This could principally occur via a private-channel, as potentially provided
582 by mixed-bipolar cells which in adults receive direct inputs only from red-
583 cones and from rods (49). However, most zebrafish bipolar cells receive
584 direct inputs from more than one cone type, presumably mixing their
585 spectral signals. Nevertheless, a PC1-like signal does filter all the way to
586 the brain where it forms the dominant Off-response (47).

587 **Primary chromatic signalling.** In natural scenes, all spectral variance that
588 is not captured by PC1 is chromatic, with any subsequent components
589 capturing progressively smaller fractions of the remaining variance in a
590 mutually orthogonal manner. Accordingly, PC2 and PC3 are maximally
591 informative about primary and secondary spectral contrasts, respectively,
592 while at the same time being uninformative both about brightness (i.e.
593 PC1), or about each other. Here, we found that zebrafish green-cones (Fig.
594 2n), as well as *Drosophila* yR7 photoreceptors, both provide a good match
595 to their respective environment’s PC2 (Fig. 6d). In the case of zebrafish,
596 this match was close to perfect: When challenged with natural spectra,
597 green-cones were highly informative about PC2, but uninformative about
598 PC1 or PC3. Accordingly, like for red-cones (discussed above), the visual
599 system would be well-served to read out the signal from green-cones in a
600 private-line at least once so as to preserve this already efficient chromatic
601 signal. Indeed, green-cones are anatomically the only cones in the
602 zebrafish retina known to have such an arrangement: two of the more than
603 twenty zebrafish bipolar cell “morpho-types”, both stratifying in the
604 traditional “Off-stratum” of the inner plexiform layer (IPL), make exclusive
605 contacts to green cones (49). Potentially in agreement, we previously

606 identified a small but well-defined population of singly colour-opponent
607 bipolar cell responses in this part of the IPL (13).

608 **Further chromatic signalling.** Beyond PCs 1 and 2, most of the
609 remaining spectral variance was captured by PC3, which presents a
610 triphasic spectral response with two zero crossings. However, neither of
611 the remaining blue- and UV-cones exhibited such a tuning. Of these, blue-
612 but not UV-cones were strongly opponent, nevertheless suggesting their
613 important role in spectral processing. Accordingly, we explored why blue-
614 cones did not directly capture PC3. For this, we returned to our horizontal
615 cell model, this time immediately optimising red- green- and blue-cones to
616 match PC1, PC2 and PC3, respectively. To complete the model, UV-
617 optimisation was left unchanged to again target its own *in vivo* tuning
618 function. Using this strategy, it was possible to produce only weakly
619 distorted red-, green- and UV-cone spectra. However, the model failed to
620 directly capture PC3 using blue-cones, and the mild relative distortion of
621 green-cone spectral tuning was sufficient to noticeably degrade their ability
622 to capture PC2 (Fig. S6h-k). This tentatively suggests that the specific
623 connectivity of the outer retina, constrained by the four principal zebrafish
624 cone-opsins, is poorly suited to additionally produce a PC3-like spectral
625 response.

626 Nevertheless, blue-cones did exhibit a single zero crossing that differed
627 from that of green-cones, meaning that two zero crossing could be readily
628 achieved in a linear model that opposed green- and blue-cone signals (Fig.
629 S5). We showed that such an arrangement would at least in theory allow
630 building a spectral filter which closely captures PC3 while producing only
631 poorly correlated responses to PC1 and PC2. Intriguingly, such a PC3-like
632 filter is in fact observed at the level of the brain, which mainly opposes UV-
633 and Red- “On” signals with spectrally intermediate blue/green “Off” signals
634 (47). However, how this brain response is set-up at the level of the retina,
635 remains unclear. Finally, a PC3-like signal could also be achieved in
636 *Drosophila* by opposing their two mid-wavelength sensitive yR7 and pR8
637 photoreceptors, however in this case the best match was achieved when in
638 addition recruiting the more broadly tuned yR8 alongside yR7 (Fig. S6d,f).

639 **A private channel for detecting UV-signals?** Remarkably, unlike red-
640 green- or blue-cones, the final output of zebrafish UV-cones appeared to
641 not be central to support dominant achromatic nor chromatic processing. In
642 fact, UV-cones also use a nearly UV-exclusive horizontal cell (H3, Figs.
643 3,4) (30, 33), likely for temporal tuning (10), while barely contributing to the
644 signals of H1 and H2 (Fig. 4d). Accordingly, outer retinal UV-circuits
645 appear to approximately signal in isolation from those of the remaining
646 cones. Similarly, direct contributions from the UV-sensitive pR7
647 photoreceptors were also not required to approximate the first three PCs
648 that emerge from the natural spectral world of *Drosophila* (Fig. 6d,e). In
649 both cases, these photoreceptors contrasted their strong, short-wavelength
650 exclusive response with weaker opposition at most other wavelengths.
651 From here, it is tempting to speculate that these UV-systems may serve to

652 *detect*, rather than necessarily to *spectrally contrast*, the presence of
653 strongly UV-biased objects against a “naturally-grey” background. Such a
654 detector would be invaluable for reporting the presence of the UV-bright
655 single-celled microorganisms when illuminated by the sun, which larval
656 zebrafish feed on (10). To our knowledge, a similarly specific visuo-
657 ecological purpose of UV-vision in *Drosophila* remains unknown. More
658 generally, UV-light can be highly informative about edges in space, as it
659 tends to accentuate objects’ silhouettes against bright backgrounds (50–
660 52).

661 In zebrafish, previous work has highlighted a key role of UV-vision across
662 the retina and brain leading to behaviour (10, 13, 24, 47, 53, 54). Most
663 notably, the retina’s acute zone (25) is dominated by UV-sensitive circuits
664 (13). Here, most bipolar cell terminals respond primarily to UV-stimulation,
665 and only some in addition respond to other wavelengths (13) – a general
666 pattern that is recapitulated also at the level of the retinal ganglion cells
667 (24) to drive a strong UV-response in the brain (47, 55, 56) which filters all
668 the way to spinal circuits (56, 57). Nevertheless, despite this profound
669 functional dominance, no anatomical study has reported the presence of
670 UV-cone-dedicated bipolar cells, as for example in the case of green-
671 cones (49) (see above). While it remains unknown if such connectivity
672 specifically exists in the acute zone, it seems clear that more broadly
673 across the retina, the signals from UV-cones are mixed with those of other
674 cones. How this connectivity serves to support the diverse visuo-
675 ecological needs of zebrafish UV-vision will be important to address in the
676 future.

677 **Regional differences in cone spectral tuning.** Unlike many other
678 aspects of larval zebrafish retinal structure (13, 24–26, 58) and function
679 (10, 13, 24), the spectral tuning of zebrafish cones was remarkably eye-
680 region invariant (Fig. S1g). Nevertheless, small but significant regional
681 variations were observed in all cone-types. Of these, the most striking
682 differences occurred in red- and green-, and to a smaller extent also in UV-
683 cones. Red-cones, and to a weaker extent also other cones, exhibited
684 relatively narrowed tuning ventrally, and broadened tunings dorsally. These
685 differences might help keeping cones within operational range despite the
686 large difference in absolute amount light driving them: bright direct skylight
687 versus dimmer reflected light from below, respectively. Next, amongst
688 green-cones, the acute-zone exhibited the strongest short-wavelength
689 response, resulting in a long-wavelength shift in their zero crossing. This
690 finding is conceptually in line with an increase in absolute light sensitivity
691 amongst UV-cones in this part of the eye (10), however a possible visuo-
692 ecological purpose of this shift remains to be established. Finally, mid-
693 wavelength opponency amongst UV-cones was strongest in the AZ and
694 ventrally, which may be linked to the behavioural need to contrast UV-
695 bright prey against a spectrally intermediate but bright background in the
696 upper-frontal parts of visual space (10, 59). In contrast, larval zebrafish
697 rarely pursue prey below or behind them (59, 60), as surveyed by dorsal
698 and nasal UV-cones, respectively.

699 Finally, we wondered how eye-region differences in cone-tunings might be
700 achieved at the level of outer retinal circuits. To explore this, we again
701 returned to our horizontal cell model, this time fitting it individually to only
702 the subsets of recordings from each of the four regions. This revealed that
703 the same anatomically established maximal connectivity matrix (Figs. 3,4)
704 served well to produce any of these regional differences by minimally
705 shifting their relative weights (Table S1). Accordingly, it seems likely that
706 the same principal horizontal cell network produces these regional
707 variations in tuning based on minor rebalancing of its relative input
708 strengths.

709

710 **METHODS**

711

712 **RESOURCE AVAILABILITY**

713 ***Lead Contact***

714 Further information and requests for resources and reagents should be
715 directed to and will be fulfilled by the Lead Contact, Tom Baden
716 (t.baden@sussex.ac.uk).

717 ***Material Availability***

718 Plasmids pBH-opn1sw2-SyGCaMP6f-pA, pBH-LCRhsp70l-SyGCaMP6f-
719 pA, pBH-thrb-SyGCaMP6f-pA, pBH-cx55.5-nlsTrpR-pA, pBH-tUAS-
720 ASAP3-pA and transgenic lines *Tg(opn1sw2:SyGCaMP6f)*,
721 *Tg(LCRhsp70l:SyGCaMP6f)*, *Tg(thrb:SyGCaMP6f)*,
722 *Tg(cx55.5:nlsTrpR,tUAS:ASAP3)*, generated in this study, are available
723 upon request to the lead contact.

724 ***Data and Code Availability***

725 Pre-processed functional 2-photon imaging data, natural imaging data,
726 EM-data, HC circuit modelling data, and associated summary statistics will
727 be made freely available via the relevant links on
728 <http://www.badenlab.org/resources> and <http://www.retinal-functomics.net>.
729 Code for the model and the statistical analysis of the experimental data is
730 available on Github ([https://github.com/berenslab/cone colour tuning](https://github.com/berenslab/cone_colour_tuning)).
731 Natural imaging datasets were published previously as part of (12, 13).

732

733 **EXPERIMENTAL MODEL AND SUBJECT DETAILS**

734 ***Animals.*** All procedures were performed in accordance with the UK
735 Animals (Scientific Procedures) act 1986 and approved by the animal
736 welfare committee of the University of Sussex. For all experiments, we
737 used 7-8 days post fertilization (*dpf*) zebrafish (*Danio rerio*) larvae. The
738 following previously published transgenic lines were used:

739 *Tg(opn1sw1:nfsBmCherry)*(33), *Tg(opn1sw1:GFP)*(61),
740 *Tg(opn1sw2:mCherry)*(62), *Tg(thrb:Tomato)*(63). In addition,
741 *Tg(opn1sw2:SyGCaMP6f)*, and *Tg(LCRhsp70l:SyGCaMP6f)*,
742 *Tg(thrb:SyGCaMP6f)*, lines were generated by injecting pBH-opn1sw2-
743 SyGCaMP6f-pA, pBH-LCRhsp70l-SyGCaMP6f-pA, or pBH-thrb-
744 SyGCaMP6f-pA. *Tg(cx55.5:nlsTrpR,tUAS:ASAP3)*, line was generated by
745 co-injecting pBH-cx55.5-nlsTrpR-pA and pBH-tUAS-ASAP3-pA plasmids
746 into single-cell stage eggs. Injected fish were out-crossed with wild-type
747 fish to screen for founders. Positive progenies were raised to establish
748 transgenic lines.

749 All plasmids were made using the Gateway system (ThermoFisher,
750 12538120) with combinations of entry and destination plasmids as follows:
751 pBH-opn1sw2-SyGCaMP6f-pA: pBH (33) and p5E-opn1sw2 (33), pME-
752 SyGCaMP6f (Yoshimatsu et al., 2020), p3E-pA(64); pBH-LCRhsp70l-
753 SyGCaMP6f-pA: pBH and p5E-LCRhsp70l, pME-SyGCaMP6f, p3E-pA;
754 pBH-thrb-SyGCaMP6f-pA: pBH and p5E-1.8thrb (63), pME-SyGCaMP6f,
755 p3E-3.2thrb (63); pBH-tUAS-ASAP3-pA: pBH and p5E-tUAS (65), pME-
756 ASAP3, p3E-pA. Plasmid p5E-LCRhsp70l was generated by inserting a
757 polymerase chain reaction (PCR)-amplified Locus Control Region (LCR)
758 for green opsins (RH2-1 to 2-4) (66) into pME plasmid and subsequently
759 inserting a PCR amplified zebrafish 0.6 kb hsp70l gene promoter region
760 (67) downstream of LCR. pME-ASAP3 was made by inserting a PCR
761 amplified ASAP2s fragment (68) and subsequently introducing L146G,
762 S147T, N149R, S150G and H151D mutations (37) in pME plasmid.

763 Animals were housed under a standard 14:10 day/night rhythm and fed
764 three times a day. Animals were grown in 0.1 mM 1-phenyl-2-thiourea
765 (Sigma, P7629) from 1 dpf to prevent melanogenesis. For 2-photon *in-vivo*
766 imaging, zebrafish larvae were immobilised in 2% low melting point
767 agarose (Fisher Scientific, BP1360-100), placed on a glass coverslip and
768 submerged in fish water. Eye movements were prevented by injection of a-
769 bungarotoxin (1 nL of 2 mg/ml; Tocris, Cat: 2133) into the ocular muscles
770 behind the eye. For some experiments, CNQX (~0.5 pl, 2 mM, Tocris, Cat:
771 1045) or meclofenamic acid sodium salt (MFA) (~0.5 pl, 5 mM, Sigma, Cat:
772 M4531) in artificial cerebro-spinal fluid (aCSF) was injected into the eye.
773

774 **METHOD DETAILS**

775 **Light Stimulation.** With fish mounted on their side with one eye facing
776 upwards towards the objective, light stimulation was delivered as full-field
777 flashes from a spectrally broad liquid waveguide with a low NA (0.59,
778 77555 Newport), positioned next to the objective at ~45°. To image
779 different regions in the eye, the fish was rotated each time to best
780 illuminate the relevant patch of photoreceptors given this stimulator-
781 geometry. The other end of the waveguide was positioned behind a
782 collimator-focussing lens complex (Thorlabs, ACL25416U-A, LD4103)
783 which collected the light from a diffraction grating that was illuminated by

784 14 spectrally distinct light-emitting diodes (LEDs) (details on LEDs below).
785 Following the an earlier design (14), the specific wavelength and relative
786 angle of each LED to the diffraction grating defined the spectrum of light
787 collected by the collimator to be ultimately delivered to the fish's eye,
788 according to:

$$789 \alpha(\lambda) = \sin^{-1}(G\lambda - \sin \beta)$$

790 where α is the angle of light incident to the diffraction grating, λ the
791 wavelength (in nm), β the first order diffraction exit angle and G the
792 diffraction grating's groove density. Moreover, each LED was individually
793 collimated (Signal Construct SML 1089 - LT-0454) and attached to a rail
794 (Thorlabs, XE25L450/M; XE25L225/M) by a 3D printed holder (available at
795 <https://github.com/BadenLab/HyperspectralStimulator>).

796
797 An Arduino Due (Arduino) and LED driver (Adafruit TCL5947) were used to
798 control and drive the LEDs, respectively. Each LED could be individually
799 controlled, with brightness defined via 12-bit depth pulse-width-modulation
800 (PWM). To time-separate scanning and stimulating epochs, a global
801 "blanking" signal was used to switch off all LEDs during 2P scanning but
802 enable them during the retrace, at line-rate of 500 Hz (see also (15, 16)).
803 The stimulator code is available at
804 <https://github.com/BadenLab/HyperspectralStimulator>.

805
806 LEDs used were: Multicomp Pro: MCL053RHC, Newark: C503B-RAN-
807 CZ0C0AA1, Roithner: B5-435-30S, Broadcom: HLMP-EL1G-130DD,
808 Roithner: LED-545-01, TT Electronics: OVLGC0C6B9, Roithner: LED-490-
809 06, Newark: SSL-LX5093USBC, Roithner: LED450-03, VL430-5-1,
810 LED405-03V, VL380-5-15, XSL-360-5E. Effective LED peak spectra as
811 measured at the sample plane were, respectively (in nm): 655, 635, 622,
812 592, 550, 516, 501, 464, 448, 427, 407, 381, 361, 360 nm. Their maximal
813 power outputs were, respectively (in μW): 1.31, 1.06, 0.96, 0.62, 1.26,
814 3.43, 1.47, 0.44, 3.67, 0.91, 0.24, 0.23, 0.04, 0.20. From here, the first ten
815 LEDs (655 – 427 nm) were adjusted to 0.44 μW , while the four UV-range
816 LEDs were set to a reduced power of 0.2 μW (407, 381, 360 nm) or 0.04
817 μW (361 nm). This relative power reduction in the UV-range was used as a
818 compromise between presenting similar power stimulation across all LEDs,
819 while at the same time ameliorating response-saturation in the UV-range
820 as a result of the UV-cones' disproportionately high light sensitivity (10,
821 24). In this regard, we took advantage of the strong spectral overlap
822 between the two shortest-wavelength LEDs (360, 361 nm) to probe this
823 wavelength range at two intensities (0.2 and 0.04 μW , respectively).

824 From here, all spectral tuning functions were based on the responses to
825 the 13 spectrally distinct LEDs, excluding the response to low-power 361
826 nm LED. This strategy yielded biologically highly plausible spectral
827 sensitivity functions in all cones that closely resembled their underlying
828 opsin's tuning when pharmacologically isolated from horizontal cells (Fig.
829 2b). Nevertheless, UV-cones weakly but consistently under-shot their opsin
830 template at the shortest tested wavelength (360 nm), hinting that they may

831 have approached their saturation point at this wavelength and power. In
832 agreement, the 0.04 μ W 361 nm LED elicited only mildly lower response-
833 amplitudes in UV-cones compared to the 0.2 μ W 360 nm LED ($R_{\text{low}} =$
834 0.88 ± 0.14 ; $R_{\text{high}} = 0.96 \pm 0.06$, errors in SD; difference $p \ll 0.001$ Wilcoxon
835 signed-rank test). In contrast, all other cones responded much more
836 weakly to the low power UV-LED: Blue-cone ($R_{\text{low}} = 0.35 \pm 0.16$; $R_{\text{high}} =$
837 0.67 ± 0.21); green-cone ($R_{\text{low}} = -0.12 \pm 0.24$; $R_{\text{high}} = 0.09 \pm 0.32$); red-cone
838 ($R_{\text{low}} = -0.02 \pm 0.27$; $R_{\text{high}} = 0.21 \pm 0.27$; all low-high pairs $p \ll 0.001$)
839 suggesting that these cones were not near their UV-saturation points.
840 Together, it therefore remains possible that measured cone-tuning
841 functions relatively underestimate UV-components, however this effect is
842 likely to be very small in non-UV-cones that dominate “traditional” colour
843 vision in zebrafish (Discussion). The exact slope of the cones’ UV-
844 response also had negligible impact on their relative matches with PCs or
845 their contributions to the HC-network (not shown), in line with an only weak
846 interdependence of the outer retina’s UV- versus red-/green-/blue-cone
847 systems (see Discussion).

848
849 **2-photon calcium and voltage imaging.** All 2-photon imaging was
850 performed on a MOM-type 2-photon microscope (designed by W. Denk,
851 MPI, Martinsried; purchased through Sutter Instruments/Science Products)
852 equipped with a mode-locked Ti:Sapphire laser (Chameleon Vision-S,
853 Coherent) tuned to 960 nm for SyGCaMP6f and ASAP3 imaging. To
854 measure HC tuning functions, we first expressed GCaMP6f in HCs.
855 However, while we observed strong light-driven calcium responses at their
856 dendritic tips, adjacent to cone terminals and thus indicative of local
857 processing, we did not observe robust calcium responses in the HC soma
858 (as a proxy of global processing). This lack of somatic calcium responses
859 could be due to a putative lack of voltage-gated calcium channels in larval
860 HC somata (unlike e.g. in adult mouse (69)). Instead, we therefore
861 measured voltage responses using the genetically encoded voltage
862 sensor, ASAP3(37), which presumably also gave a more direct readout of
863 HC global function. We used two fluorescence detection channels for
864 SyGCaMP6f/ASAP3 (F48x573, AHF/Chroma) and mCherry (F39x628,
865 AHF/Chroma), and a water immersion objective (W Plan-Apochromat
866 20x/1,0 DIC M27, Zeiss). For image acquisition, we used custom-written
867 software (ScanM, by M. Mueller, MPI, Martinsried and T. Euler, CIN,
868 Tuebingen) running under IGOR pro 6.3 for Windows (Wavemetrics).
869 Recording configurations were as follows: UV-cone SyGCaMP6f 128x128
870 pixels (2 ms per line, 3.9 Hz) or 256x256 pixels (2 ms per line, 1.95 Hz); all
871 other cones SyGCaMP6f and horizontal cell ASAP3 256x256 pixels (2 ms
872 per line, 1.95 Hz).

873
874 **Pre-processing and extraction of response amplitudes of 2-photon**
875 **data.** Regions of interest (ROIs), corresponding to individual presynaptic
876 cone terminals were defined automatically based on local thresholding of
877 the recording stack’s standard deviation (s.d., typically > 25) projection
878 over time, followed by filtering for size and shape using custom written

879 scripts running under IGOR Pro 6.3 (Wavemetrics), as used previously in
880 (Yoshimatsu et al., 2020). Specifically, only ellipsoidal ROIs (<150%
881 elongation) of size 2-5 μm^2 were further analyzed. For ASAP3 recordings,
882 ROIs were manually placed to follow the shape of individual HC somata.
883 Calcium or voltage traces for each ROI were extracted and z-normalized
884 based on the time interval 1-6 s at the beginning of recordings prior to
885 presentation of systematic light stimulation. A stimulus time marker
886 embedded in the recording data served to align the traces relative to the
887 visual stimulus with a temporal precision of 2 ms.
888 Following the approach used in (70), a quality criterium (QC) of how well a
889 cell responded to a stimulus were computed as

$$890 \quad QC = \frac{\text{Var}[\langle C \rangle_r]_t}{\text{Var}[\langle C \rangle_t]_r}$$

891 where C is the T by R response matrix (time samples by stimulus
892 repetitions) and $\langle \rangle_x$ and $\text{Var}[\]_x$ denote the mean and variance across the
893 indicated dimension, respectively. If all trials are identical such that the
894 mean response is a perfect representative of the response, QC is equal to
895 1. If all trials are random with fixed variance, QC is equal to 1/R. For further
896 analysis, we used only cells that responded well to the stimulus (QC >0.4
897 for SyGCaMP6f or >0.32 for ASAP3) (see also SFig. 2b)

898
899 After filtering out poorly responsive cells using QC, outliers were removed
900 using principal component analysis. Because in all cone types, PC1
901 explained >80% variance of the data, we computed the loading values of
902 the principal component 1 of cone tuning function within each cone type
903 and defined outliers as the cones with PC1 loading below 1.25 times the
904 length of the 97 percentile departure from the mean.

905 To extract response amplitudes to each stimulus wavelength, an
906 exponential curve was fit to the entire rising (or falling, for hyperpolarising
907 responses) phase during each stimulus presentation, with the maximum
908 value of the fitted curve was taken as the response amplitude. Because
909 cones are intrinsically “Off-cells” (i.e. hyperpolarize to light) we then sign-
910 inverted extracted amplitude values such that Off-responses would yield
911 positive amplitude readings, and vice versa for On-responses. However,
912 for voltage imaging, because ASAP3 fluorescence intensity increases as
913 cells hyperpolarize, we preserved the polarity of the response amplitudes.

914
915 **Immunostaining and confocal imaging.** Larval zebrafish (7-8 dpf) were
916 euthanised by tricane overdose and then fixed in 4% paraformaldehyde
917 (PFA, Agar Scientific, AGR1026) in PBS for 30 min at room temperature.
918 After three washes in PBS, whole eyes were enucleated and the cornea
919 was removed by hand using the tip of a 30 G needle. Dissected and fixed
920 samples were treated with PBS containing 0.5% TritonX-100 (Sigma,
921 X100) for at least 10 mins and up to 1 day, followed by the addition of
922 primary antibodies. After 3-5 days incubation at 4°C, samples were
923 washed three times with PBS 0.5% TritonX-100 solution and treated with

924 secondary antibodies. After one day incubation, samples were mounted in
925 1% agar in PBS on a cover slip and subsequently PBS was replaced with
926 mounting media (VectaShield, H-1000) for imaging. For HC imaging (Fig.
927 S6c-f), the retina was flat-mounted with the photoreceptors facing to the
928 cover slip. For cone side-view imaging (Fig. S6a), the lens was kept
929 attached the retina to maintain the spherical shape of the retina, with the
930 whole “retina-ball” mounted with the lens side facing to the cover slip. All
931 presented data was imaged in the acute zone.

932 Primary antibodies were zpr-1 antibody (mouse, 1:100, ZIRC). Secondary
933 antibodies were DyLight647 anti-mouse (Donkey, 1:500, Jackson
934 Immunoresearch Laboratories). Confocal image stacks were taken on a
935 TSC SP8 (Leica) with a 63x oil immersion objective (HC PL APO CS2,
936 Leica). Typical voxel size was 90 nm and 0.5 μ m in xy and z, respectively.
937 Contrast, brightness and pseudo-colour were adjusted for display in Fiji
938 (NIH).

939 To sparsely label HCs, plasmids pCx55.5:Gal4 and pUAS:MYFP were co-
940 injected into one-cell stage eggs (71).

941 **UV-cone ablation.** Larval zebrafish were immersed in fish water
942 containing 10 mM Metronidazole (Met) for 2 hours to ablate nfsB-
943 expressing UV-cones. Following Met treatment, zebrafish were transferred
944 into fish water without Met and fed regularly until used for two-photon
945 imaging.

946 **Electron-microscopy data acquisition, reconstruction and annotation.**

947 A larval zebrafish (8 dpf) was euthanised by tricane overdose and then a
948 small incision on a cornea was made using 30G needle in a fixative
949 solution containing 4% glutaraldehyde (AGR1312, Agar Scientific,) in
950 0.12M cacodylate buffer, pH 7.4. The tissue was immediately transferred
951 into a 1.5 ml tube with the fixative, centrifuged at 3,000 rpm for 3 min, and
952 further fixed in the fixative over-night on a shaker at room temperature.
953 Subsequently, the tissue was washed 3 times in 0.12M cacodylate buffer,
954 pH7.4 and incubated in a solution containing 1.5% potassium ferrocyanide
955 and 2% osmium tetroxide (OsO₄) in 0.1M cacodylate buffer (0.66% lead in
956 0.03M aspartic acid, pH 5.5) for 1 hour. After washing, the tissue was
957 placed in a freshly made thiocarbohydrazide solution (0.1g TCH in 10 ml
958 double-distilled H₂O heated to 60 C for 1 h) for 20 min at room
959 temperature (RT). After another rinse, at RT, the tissue was incubated in
960 2% OsO₄ for 30 min at RT. The samples were rinsed again and stained *en*
961 *bloc* in 1% uranyl acetate overnight at 40 C, washed and stained with
962 Walton’s lead aspartate for 30 min. After a final wash, the retinal pieces
963 were dehydrated in a graded ice-cold alcohol series, and placed in
964 propylene oxide at RT for 10 min. Finally, the sample was embedded in
965 Durcupan resin. Semi-thin sections (0.5 -1 μ m thick) were cut and stained
966 with toluidine blue, until the fiducial marks (box) in the GCL appeared. The
967 block was then trimmed and mounted in a Serial-blockface scanning
968 electron microscope (GATAN/Zeiss, 3View). Serial sections were cut at 50

969 nm thickness and imaged at an xy resolution of 5 nm. Two tiles, each
970 about 40 μm x 40 μm with an overlap of about 10%, covering the entire
971 photoreceptor and horizontal cell layers in a side view at the acute zone
972 were obtained. The image stacks were concatenated and aligned using
973 TrackEM (NIH). The HCs and cones were traced or painted using the
974 tracing and painting tools in TrackEM2 (72).

975 **Clustering of HCs in EM and Confocal data.** To validate the ad hoc
976 group assignment based on UV contacts (HC area) and R/G contacts for
977 the electron microscopy (Fig. 3h,i) and confocal data (Fig. S3g) we used
978 Mixture of Gaussian (MoG) clustering on all extracted features. These
979 features (area size, number of contacts to R/G, B, U, for EM and area size,
980 tip density, number of contacts to R, G, B/U for CM) were z-normalized and
981 clustered in the same framework as the HC recordings (see below). The
982 MoG clusters did coincide with the ad hoc group assignment.

983 **Opsin Templates and log transforms.** For the log-transformed opsin
984 templates (Fig. 1f, 2b) we assumed a baseline activation (represented by b
985 in Eq. 2) and fit a linear transformation to take the arbitrary scaling of the
986 recordings into account. We then optimized the function $f_{a,b,c}$ to minimize
987 the mean squared error (MSE) between $f_{a,b,c}(\text{opsin})$ and the data of the
988 HC block condition for each cone type:

$$989 \quad a, b, c = \underset{a,b,c}{\operatorname{argmin}} \operatorname{MSE}(f_{a,b,c}(\text{opsin}), y) \quad (1)$$

990 where y is the mean of the HC block condition and f is the function

$$991 \quad f_{a,b,c}(x) = a \cdot \log(x + b) + c. \quad (2)$$

992 For the optimization we used the python package `scipy.optimize.minimize`
993 (version 1.4.1). The inverse of this procedure is shown in Fig. S4a, where
994 the mean of HC block condition is fitted in the same way to the opsin
995 curves of each cone with the function:

$$996 \quad f'_{\alpha',b',c'}(x) = \alpha' \cdot \exp(b' \cdot x) + c' \quad (3)$$

997 The data distribution (25 and 50 and 75 percentiles) is then calculated by
998 passing each individual HC block recording through the optimized function
999 f' .

1000 **Model of cone and HC interaction.** We modelled cone-HC interactions as
1001 a linear model and included the established (Fig. 3k) connectivity pattern
1002 for the three types of HC as a (3x4) connectivity matrix W where w_{ij}
1003 indicates connection strength from cone type j to HC type i . Further, we
1004 assumed the feedback strength per connection of each HC type to be
1005 constant for all cones and defined it as a diagonal matrix A . To compute
1006 the effective feedback, this matrix is then weighted by the relative
1007 connection strength per cone and HC, represented in a (4x3) matrix F with
1008 $f_{ij} = \frac{w_{ij}}{\sum_k w_{jk}}$. This represents the strength from HC type j to cone of type i .

1009 Hereby we assume a symmetric connectivity pattern which is justified by
1010 the symmetrical cone mosaic in zebrafish. With these definitions, we can
1011 formulate the model recurrently as following:

1012 The inputs to the HCs is defined as

$$1013 H_{in}(\lambda) = W \cdot \kappa(\lambda),$$

1014 where $\kappa(\lambda)$ represents the raw activity in the synapse, which still has to be
1015 shifted according to the baseline. The summed outputs of the HCs are
1016 computed as

$$1017 H_{out}(\lambda) = F \cdot A \cdot H_{in}(\lambda),$$

1018 Finally, the raw activity in the synapses is computed as

$$1019 \kappa(\lambda) = o(\lambda) - H_{out}(\lambda)$$

1020 where $o(\lambda)$ represents the wavelength dependent opsin activation.

1021 The same formulas hold for computing the baseline of the cones, for which
1022 $o(\lambda)$ was set to 1, which accords to the applied normalization on the
1023 recorded data. The final output of the model are the tuning curves κ shifted
1024 to the cone specific baselines and normalized.

1025 The same normalization procedure was applied to the shown HC spectra,
1026 which are the normalized spectra $H_{in}(\lambda)$.

1027 In the reduced models, in which we only included specific types of HCs, we
1028 set the corresponding entries in the weight matrix W to zero but did not
1029 change the model otherwise.

1030 *Model input.* To extract the cone tuning curves from the experimental data
1031 for the model, we computed the mean amplitude of each bright and dark
1032 three seconds interval but excluded in each interval the first second as
1033 adaption time. We then took for every individual trace the difference of
1034 each bright interval to its preceding dark interval based on these means.
1035 Finally, we averaged over these values for each cone type and
1036 experimental condition and, by assuming smooth tuning functions,
1037 interpolated (using the scipy function `scipy.interpolate.interp1d`) the data to
1038 an equidistant resolution of 1nm.

1039 As input to our model we took the normalized traces of the blocked HC
1040 condition. This normalization can be interpreted as a maximal dark current
1041 of 1 and a minimal current of 0 during activation. The input acted as "opsin-
1042 sensitivity" curves $o(\lambda)$ of the cones. We decided to use these curves
1043 instead of the theoretical available opsin tuning curves since we have a
1044 pure linear model and as shown in Fig. 2b these traces are a good proxy
1045 for the log-transformed opsin templates, which is the effective activation for
1046 this linear model. All spectral tuning curves of the cones were normalized
1047 to have a maximal absolute value of one.

1048

1049 *Fitting procedure.* We used the Sequential Neural Posterior Estimation
1050 method (also called SNPE-B) described in (36) (code available at
1051 <https://github.com/mackelab/delfi>, version: 0.5.1) with small modifications
1052 which were already applied in (73) to fit our model.

1053 In brief, SNPE-B draws parameters $\{\theta_i\}_{i \in I}$ over several rounds
1054 $r = 1, \dots, R$ from a (proposal) prior $\tilde{p}_r(\theta)$ and evaluates the model for
1055 these parameters. For the evaluations $e_i(\theta_i)$ the discrepancy function
1056 $x_i(e_i) = D(e_i)$ is computed and a mixture density network (MDN)
1057 $q_\phi(\theta, x)$ is trained on the data pairs $\{(\theta_i, x_i)\}_{i \in I}$. The posterior $p_r(\theta|x_0)$ is
1058 then calculated as $q_\phi(\theta|x = x_0)$ and used as a new proposal prior in the
1059 next sampling round: $\tilde{p}_{r+1}(\theta) = p_r(\theta|x_0)$. We took the MSE between
1060 model output and the data as discrepancy function. This implies $x_0 = 0$,
1061 but as our data is noisy, our model cannot get to a MSE of zero. This would
1062 mean, that the MDN has to extrapolate to unreached discrepancy values,
1063 which could lead to an unstable behaviour. As a consequence, we took as
1064 x_0 the 0.01-percentile of $\{x_i\}_{i \in I}$ in each round. This evaluation of
1065 $q_\phi(\theta|x = x_0)$ can be understood as the posterior over the parameters for
1066 the "best possible" model evaluations. Testing for different percentiles in a
1067 reasonable range did not change the results. We took the same approach
1068 for setting an adaptive bandwidth for the kernel (see also (73)). As for a
1069 few models the posteriors became slightly worse after some rounds, we
1070 compared post-hoc the posterior distributions of each round and took the
1071 one with the smallest 1-percentile of its samples.

1072 We ran SNPE-B over five rounds, with 200,000 samples per round. The
1073 prior was a multivariate normal distribution with mean $\mathbf{1}_n$ and covariance
1074 $0.25 \cdot Id_n$, where n is the number of model parameters, ranging from 11
1075 (all HCs) to 3 (only H2). We chose three Gaussian components for the
1076 MoG and a MDN with two hidden layers with 100 nodes each. In each
1077 round the network was trained for 600 epochs with a minimum batch size
1078 of 500 and continuous learning started in round two. To let the MDN focus
1079 on regions of low discrepancy, we used a combined Uniform-Half-
1080 Gaussian kernel which was constant 1 up to x_0 and decayed then as a half
1081 Gaussian. The scale of the Half-Gaussian part was in each round chosen
1082 as the 20-percentile of the discrepancy values. For the presented tuning
1083 curves 100,000 samples were drawn from the final posterior and the model
1084 evaluated.

1085 **HC clustering based on spectral tuning.** To identify functional clusters
1086 we used a Mixture of Gaussians model (sklearn.mixture.GaussianMixture,
1087 version 0.21.2) with three components and diagonal covariance matrices
1088 on the pre-processed tuning curves ($n = 86$) which were additionally
1089 normalized to have maximal value of one. Aiming for a stable clustering,
1090 we ran the algorithm 1,000 times with different random seeds and chose

1091 the ones with the smallest BIC and under these chose the partition which
1092 appeared most often. The different runs did not change the general shape
1093 of the cluster means, but the specific assignment was variable for some
1094 traces. With this procedure we got a partition with $n = 12, 19, 55$ elements,
1095 which were allocated to the known functional tunings for HCs of adult
1096 zebrafish (30, 34).

1097 **Natural Imaging Data Analysis.** The hyperspectral data were element-
1098 wise multiplied with a deuterium light source derived correction curve [S.x].
1099 The data were restricted to the domain of 360-650 nm and z-normalised
1100 within a given scan. Here, the long-wavelength end of the domain was
1101 decided based on the long-wavelength opsin absorption curve; the short-
1102 wavelength end was dictated by the sensitivity of the spectrometer. The
1103 hyperspectral PCs were obtained using the scikit-learn 0.22.1
1104 implementation of the Principal Component Analysis algorithm. Only the
1105 first three components are displayed.

1106 Hyperspectral measurement points were spatially aligned within the scan
1107 according to the scan raster (see (12, 13) for details). Pixel brightness is
1108 the projection of a given PC, or mean of the convolution with the opsin
1109 absorption or the observed cone response curves respectively. Presented
1110 images were smoothed using a Gaussian filter ($\sigma = 2\text{px}$). Sum of
1111 Squares difference was taken between pairs of z-normalised images as
1112 well as their negatives. The lowest Sum of Squares (=highest correlation,
1113 either with the original or the negative) is displayed. Smoothing did not
1114 significantly affect this measure.

1115 To statistically compare scene reconstructions by different sets of tuning
1116 functions (Fig. S6a-c), we used two parallel strategies. First, we computed
1117 the correlation coefficient between reconstructions by the different
1118 channels (e.g. *in vivo* red cone vs. green cone) as indicated for each of $n =$
1119 30 scenes, thus yielding 30 correlation coefficients for each combination of
1120 channels in each condition. Amongst each comparison we then computed
1121 the mean and SD, as shown.

1122 Second, to capture the multivariate dependence directly, we computed the
1123 mutual information under Gaussian assumption,
1124 $MI = \sum_i h(x_i) - h(x) \sim \log \det[2 \pi e C]$, where C is the correlation matrix
1125 of the scene representations in the different channels (e.g. 4x4 *in vivo*: red-
1126 , green-, blue-, UV-cone). As the diagonal of C is constant and equal to 1,
1127 the mutual information is proportional to the latter quantity. We normalized
1128 this quantity by the mutual information of the opsin set of tuning functions.

1129 **Linking opsin- and photoreceptor-spectra to principal components.**
1130 Measured *in vivo* spectra of cones and their underlying log-transformed
1131 opsin templates (Fig. 1f) were linearly combined to provide least-squares
1132 fits to the respective underwater spectral PCs (Figs. 5n, 6d, Figs. S5,6).
1133 The same procedure was also used to match *Drosophila* R7/8 spectra (Fig.
1134 6c, from (11)) to the PCs that emerged from natural distribution of light
1135 above the water. Next, to compare the expected responses of *in vivo*

1136 photoreceptors, their linear combinations (in case of PC3, see below), as
1137 well as their respective log-opsin constructs to natural light, individual
1138 natural light pixel spectra ($n = 30,000$) were multiplied with the respective
1139 sensitivity curves. In each case, pixel-spectra were first z-normalised within
1140 the scene, and products were summed over all wavelengths. This
1141 procedure produced 'responses' (Fig. 6a), which were plotted against the
1142 respective loadings of each spectrum onto PC1, PC2 and PC3 (in rows 1,
1143 2 and 3, respectively). From here, scene-wise summary statistics were
1144 computed based on Spearman correlation coefficients (Fig. 6b,e).

1145 To arrive at *in vivo* photoreceptor combinations that best approximated
1146 PC3s zebrafish: Fig. S5a-c, *Drosophila*: Fig. S6e,f), we assessed the
1147 spectral matches to them by several plausible linear combinations of *in-*
1148 *vivo* photoreceptor tunings based on least squares. In both cases, the best
1149 fits required opposing the two spectrally intermediate receptors. For
1150 zebrafish, this "GB-fit" performed as well as any combination of more
1151 complex fits that in addition used red- or UV-cones, so we used this
1152 simplest GB-fit for further analysis. In case of *Drosophila*, best performance
1153 required also adding the long-wavelength sensitive receptor to yield an
1154 yR8+yR7-pR8 axis (short: "yyp8"). In each case, performance as shown in
1155 Figs. S5c and Fig. S6f (top) was evaluated based on the mean scene-wise
1156 Spearman correlation coefficient between the resultant spectral axis, as
1157 described above. The weights needed to build these PC3-like tunings
1158 based on photoreceptor types are plotted below as abs(max)-normalised
1159 for better comparison.

1160

1161 QUANTIFICATION AND STATISTICAL ANALYSIS

1162 **Statistics.** No statistical methods were used to predetermine sample size.
1163 Owing to the exploratory nature of our study, we did not use randomization
1164 or blinding.

1165 We used Generalized Additive Models (GAMs) to analyse the relationships
1166 between wavelength and cone activity under different experimental
1167 conditions (Fig. 2d-h, Fig. S2). GAMs can be understood as an extension
1168 to the generalized linear model by allowing linear predictors, which depend
1169 on smooth functions of the underlying variables (74). We used the mgcv-
1170 package (version 1.8-31) in R on an Ubuntu 16.04.6 LTS workstation with
1171 default parameters. We modelled the dependence of the variable of
1172 interest as a smooth term with 13 degrees of freedom. The models
1173 explained ~59-82% of the deviance. Statistical significance for differences
1174 between the dependence of activation in the different experimental
1175 conditions were obtained using the plot_diff function of the itsadug-
1176 package for R (version 2.3). Significance of opponency (Fig. S1g) and zero
1177 crossings of the tuning curves (Fig. 1f, Fig. S1g) were also calculated
1178 based on GAMs with "zone" as an additional predictive variable and
1179 grouping where applicable.

1180 REFERENCES

1181

- 1182 1. G. Buchsbaum, a Gottschalk, Trichromacy, opponent colours coding and optimum colour information transmission in
1183 the retina. *Proc. R. Soc. Lond. B. Biol. Sci.* **220**, 89–113 (1983).
- 1184 2. C. C. Chiao, T. W. Cronin, D. Osorio, Color signals in natural scenes: characteristics of reflectance spectra and effects
1185 of natural illuminants. *J. Opt. Soc. Am. A. Opt. Image Sci. Vis.* **17**, 218–224 (2000).
- 1186 3. A. Lewis, L. Zhaoping, Are cone sensitivities determined by natural color statistics? *J. Vis.* **6**, 285–302 (2006).
- 1187 4. T. Baden, D. Osorio, The Retinal Basis of Vertebrate Color Vision. *Annu. Rev. Vis. Sci.* **5**, 177–200 (2019).
- 1188 5. J. J. Atick, Z. Li, A. N. Redlich, Understanding Retinal Color Coding from First Principles. *Neural Comput.* (1992),
1189 doi:10.1162/neco.1992.4.4.559.
- 1190 6. E. P. Simoncelli, B. A. Olshausen, Natural image statistics and neural representation. *Annu Rev Neurosci.* **24**, 1193–
1191 1216 (2001).
- 1192 7. H. B. H. Barlow, in *Sensory Communication* (1961;
1193 [http://www.trin.cam.ac.uk/horacebarlow/21.pdf%5Cnhttp://redwood.berkeley.edu/w/images/f/fd/02-barlow-pr-
1194 1954.pdf](http://www.trin.cam.ac.uk/horacebarlow/21.pdf%5Cnhttp://redwood.berkeley.edu/w/images/f/fd/02-barlow-pr-1954.pdf)), pp. 217–234.
- 1195 8. A. Meier, R. Nelson, V. P. Connaughton, Color Processing in Zebrafish Retina. *Front. Cell. Neurosci.* (2018),
1196 doi:10.3389/fncel.2018.00327.
- 1197 9. J. H. Bollmann, The Zebrafish Visual System: From Circuits to Behavior. *Annu. Rev. Vis. Sci.* **5**, 269–293 (2019).
- 1198 10. T. Yoshimatsu, C. Schröder, N. E. Nevala, P. Berens, T. Baden, Fovea-like Photoreceptor Specializations Underlie
1199 Single UV Cone Driven Prey-Capture Behavior in Zebrafish. *Neuron* (2020), doi:10.1016/j.neuron.2020.04.021.
- 1200 11. S. L. Heath, M. P. Christenson, E. Oriol, M. Saavedra-Weisenhaus, J. R. Kohn, R. Behnia, Circuit Mechanisms
1201 Underlying Chromatic Encoding in Drosophila Photoreceptors. *Curr. Biol.* **30**, 264-275.e8 (2020).
- 1202 12. N. E. Nevala, T. Baden, A low-cost hyperspectral scanner for natural imaging and the study of animal colour vision
1203 above and under water. *Sci. Rep.* **9**, 10799 (2019).
- 1204 13. M. J. Y. Zimmermann, N. E. Nevala, T. Yoshimatsu, D. Osorio, D.-E. Nilsson, P. Berens, T. Baden, Zebrafish
1205 Differentially Process Color across Visual Space to Match Natural Scenes. *Curr. Biol.* **28**, 2018-2032.e5 (2018).
- 1206 14. G. Belušič, M. Ilič, A. Meglič, P. Piriš, J. Mogdans, S. L. Coombs, V. Daneu, B. Chann, R. Huang, T. Fujikado, A fast
1207 multispectral light synthesiser based on LEDs and a diffraction grating. *Sci. Rep.* **6**, 32012 (2016).
- 1208 15. T. Euler, K. Franke, T. Baden, in *Neuromethods* (2019).
- 1209 16. M. J. Y. Zimmermann, A. Maia Chagas, P. Bartel, S. Pop, L. L. Prieto-Godino, T. Baden, LED Zappelin': An open
1210 source LED controller for arbitrary spectrum visual stimulation and optogenetics during 2-photon imaging. *HardwareX*
1211 (2020), doi:10.1016/j.ohx.2020.e00127.
- 1212 17. E. Dreosti, B. Odermatt, M. M. Dorostkar, L. Lagnado, A genetically encoded reporter of synaptic activity in vivo. *Nat.*
1213 *Methods.* **6**, 883–9 (2009).
- 1214 18. E. Raviola, N. B. Gilula, Gap junctions between photoreceptor cells in the vertebrate retina. *Proc. Natl. Acad. Sci. U.*
1215 *S. A.* (1973), doi:10.1073/pnas.70.6.1677.
- 1216 19. W. B. Thoreson, S. C. Mangel, Lateral interactions in the outer retina. *Prog. Retin. Eye Res.* **31**, 407–441 (2012).
- 1217 20. T. T. Euler, S. S. Haverkamp, T. T. Schubert, T. Baden, Retinal Bipolar Cells: Elementary Building Blocks of Vision.
1218 *Nat. Rev. Neurosci.* **15**, 507–519 (2014).
- 1219 21. T. Branchek, The development of photoreceptors in the zebrafish, *Brachydanio rerio*. II. Function. *J. Comp. Neurol.*
1220 (1984), doi:10.1002/cne.902240110.
- 1221 22. J. Bilotta, S. Saszik, S. E. Sutherland, Rod contributions to the electroretinogram of the dark-adapted developing
1222 zebrafish. *Dev. Dyn.* **222**, 564–570.
- 1223 23. V. Y. Arshavsky, T. D. Lamb, E. N. Pugh, G Proteins and Phototransduction. *Annu. Rev. Physiol.* **64**, 153–87 (2002).
- 1224 24. M. Zhou, J. Bear, P. A. Roberts, F. K. Janiak, J. Semmelhack, T. Yoshimatsu, T. Baden, Zebrafish Retinal Ganglion
1225 Cells Asymmetrically Encode Spectral and Temporal Information across Visual Space. *Curr. Biol.* (2020),
1226 doi:10.1016/j.cub.2020.05.055.
- 1227 25. E. A. Schmitt, J. E. Dowling, Early retinal development in the zebrafish, *Danio rerio*: light and electron microscopic
1228 analyses. **404**, 515–36 (1999).
- 1229 26. Y. Kölsch, J. Hahn, A. Sappington, M. Stemmer, A. M. Fernandes, T. O. Helmbrecht, S. Lele, S. Butrus, E. Laurell, I.
1230 Arnold-Ammer, K. Shekhar, J. R. Sanes, H. Baier, *Neuron*, in press, doi:10.1016/j.neuron.2020.12.003.
- 1231 27. C. Schröder, J. Oesterle, P. Berens, T. Yoshimatsu, T. Baden, *bioRxiv*, in press, doi:10.1101/2021.02.24.432674.
- 1232 28. D. M. Schneeweis, J. L. Schnapf, Photovoltage of rods and cones in the macaque retina. *Science (80-.).* **#19;268**,
1233 1053–1056 (1995).
- 1234 29. J. L. Schnapf, B. J. Nunn, M. Meister, D. A. Baylor, Visual transduction in cones of the monkey *Macaca fascicularis*. *J.*
1235 *Physiol.* **427**, 681–713 (1990).
- 1236 30. L. J. Klaassen, W. de Graaff, J. B. Van Asselt, J. Klooster, M. Kamermans, Specific connectivity between
1237 photoreceptors and horizontal cells in the zebrafish retina. *J. Neurophysiol.* **116**, 2799–2814 (2016).
- 1238 31. C. A. Chapot, T. Euler, T. Schubert, How do horizontal cells 'talk' to cone photoreceptors? Different levels of
1239 complexity at the cone-horizontal cell synapse. *J. Physiol.* **595**, 5495–5506 (2017).
- 1240 32. Y. N. Li, J. I. Matsui, J. E. Dowling, Specificity of the horizontal cell-photoreceptor connections in the zebrafish (*Danio*
1241 *rerio*) retina. *J. Comp. Neurol.* **516**, 442–53 (2009).
- 1242 33. T. Yoshimatsu, F. D. F. D. O'razi, C. R. C. R. C. Gamlin, S. C. Suzuki, A. Suli, D. Kimelman, D. W. D. W. Raible,
1243 R. O. R. O. Wong, Presynaptic partner selection during retinal circuit reassembly varies with timing of neuronal
1244 regeneration in vivo. *Nat. Commun.* **7**, 10590 (2016).

- 1245 34. V. P. Connaughton, R. Nelson, Spectral Responses in Zebrafish Horizontal Cells Include a Tetraphasic Response and
1246 a Novel UV-Dominated Triphasic Response. *J. Neurophysiol.* **104**, 2407–2422 (2010).
- 1247 35. V. P. Connaughton, D. Graham, R. Nelson, Identification and morphological classification of horizontal, bipolar, and
1248 amacrine cells within the zebrafish retina. *J. Comp. Neurol.* **477**, 371–385 (2004).
- 1249 36. J. M. Lueckmann, P. J. Gonçalves, G. Bassetto, K. Öcal, M. Nonnenmacher, J. H. Mackey, in *Advances in Neural*
1250 *Information Processing Systems* (2017).
- 1251 37. V. Villette, M. Chavarha, I. K. Dimov, J. Bradley, L. Pradhan, B. Mathieu, S. W. Evans, S. Chamberland, D. Shi, R.
1252 Yang, B. B. Kim, A. Ayon, A. Jalil, F. St-Pierre, M. J. Schnitzer, G. Bi, K. Toth, J. Ding, S. Dieudonné, M. Z. Lin,
1253 Ultrafast Two-Photon Imaging of a High-Gain Voltage Indicator in Awake Behaving Mice. *Cell* (2019),
1254 doi:10.1016/j.cell.2019.11.004.
- 1255 38. C. Schnaitmann, M. Pagni, D. F. Reiff, Color vision in insects: insights from *Drosophila*. *J. Comp. Physiol. A*
1256 *Neuroethol. Sensory, Neural, Behav. Physiol.* **206** (2020), pp. 183–198.
- 1257 39. G. D. Field, J. L. Gauthier, A. Sher, M. Greschner, T. A. Machado, L. H. Jepson, J. Shlens, D. E. Gunning, K.
1258 Mathieson, W. Dabrowski, L. Paninski, A. M. Litke, E. J. Chichilnisky, Functional connectivity in the retina at the
1259 resolution of photoreceptors. *Nature*. **467**, 673–7 (2010).
- 1260 40. D. M. Dacey, Circuitry for color coding in the primate retina. *Proc.R.Soc.Lond.B.* **93**, 582–588 (1996).
- 1261 41. O. S. Packer, J. Verweij, P. H. Li, J. L. Schnapf, D. M. Dacey, Blue-yellow opponency in primate S cone
1262 photoreceptors. *J. Neurosci.* **30**, 568–572 (2010).
- 1263 42. W. I. L. Davies, S. P. Collin, D. M. Hunt, Molecular ecology and adaptation of visual photopigments in craniates. *Mol.*
1264 *Ecol.* (2012), , doi:10.1111/j.1365-294X.2012.05617.x.
- 1265 43. J. M. Musser, D. Arendt, Loss and gain of cone types in vertebrate ciliary photoreceptor evolution. *Dev. Biol.* (2017), ,
1266 doi:10.1016/j.ydbio.2017.08.038.
- 1267 44. M. Kamermans, B. W. van Dijk, H. Spekrijse, Color opponency in cone-driven horizontal cells in carp retina. Aspecific
1268 pathways between cones and horizontal cells. *J. Gen. Physiol.* **97**, 819–43 (1991).
- 1269 45. K. Y. Wong, J. E. Dowling, Retinal bipolar cell input mechanisms in giant danio. III. ON-OFF bipolar cells and their
1270 color-opponent mechanisms. *J. Neurophysiol.* **94**, 265–72 (2005).
- 1271 46. M. Vorobyev, D. Osorio, Receptor noise as a determinant of colour thresholds. *Proc. R. Soc. B Biol. Sci.* (1998),
1272 doi:10.1098/rspb.1998.0302.
- 1273 47. P. Bartel, F. K. Janiak, D. Osorio, T. Baden, Colourfulness as a possible measure of object proximity in the larval
1274 zebrafish brain. *Curr. Biol.* **31**, R235–R236 (2021).
- 1275 48. C. R. Sharkey, J. Blanco, M. M. Leibowitz, D. Pinto-Benito, T. J. Wardill, The spectral sensitivity of *Drosophila*
1276 photoreceptors. *Sci. Rep.* **10**, 1–13 (2020).
- 1277 49. Y. N. Li, T. Tsujimura, S. Kawamura, J. E. Dowling, Bipolar cell-photoreceptor connectivity in the zebrafish (*Danio*
1278 *rerio*) retina. *J. Comp. Neurol.* **520**, 3786–802 (2012).
- 1279 50. C. Tedore, D. E. Nilsson, Avian UV vision enhances leaf surface contrasts in forest environments. *Nat. Commun.* **10**,
1280 238 (2019).
- 1281 51. T. W. Cronin, M. J. Bok, Photoreception and vision in the ultraviolet. *J. Exp. Biol.* **219**, 2790–2801 (2016).
- 1282 52. Y. Qiu, Z. Zhao, D. Klindt, M. Kautzky, K. P. Szatko, F. Schaeffel, K. Rifai, K. Franke, L. Busse, T. Euler, *bioRxiv*, in
1283 press, doi:10.1101/2020.12.08.416172.
- 1284 53. I. N. Flamarique, I. Novales Flamarique, I. N. Flamarique, Diminished foraging performance of a mutant zebrafish with
1285 reduced population of ultraviolet cones. *Proc. Biol. Sci.* **283**, 20160058 (2016).
- 1286 54. I. Novales Flamarique, Opsin switch reveals function of the ultraviolet cone in fish foraging. *Proc. R. Soc. B Biol. Sci.*
1287 **280**, 20122490–20122490 (2012).
- 1288 55. D. A. Guggiana Nilo, C. Riegler, M. Hübener, F. Engert, Distributed chromatic processing at the interface between
1289 retina and brain in the larval zebrafish. *Curr. Biol.* **0** (2021), doi:10.1016/j.cub.2021.01.088.
- 1290 56. C. Fornetto, N. Tiso, F. S. Pavone, F. Vanzi, Colored visual stimuli evoke spectrally tuned neuronal responses across
1291 the central nervous system of zebrafish larvae. *BMC Biol.* **18**, 1–17 (2020).
- 1292 57. F. . Janiak, P. Bartel, M. Bale, T. Yoshimatsu, E. H. Komulainen, M. Zhou, K. Staras, L. L. Prieto-Godino, T. Euler, M.
1293 Maravall, T. Baden, *Divergent excitation two photon microscopy for 3D random access mesoscale imaging at single*
1294 *cell resolution* (Cold Spring Harbor Laboratory, 2019; <https://www.biorxiv.org/content/10.1101/821405v1>).
- 1295 58. E. Robles, E. Laurell, H. Baier, The Retinal Projectome Reveals Brain-Area-Specific Visual Representations
1296 Generated by Ganglion Cell Diversity. *Curr. Biol.* **24**, 2085–96 (2014).
- 1297 59. D. S. Mearns, J. C. Donovan, A. M. Fernandes, J. L. Semmelhack, H. Baier, Deconstructing Hunting Behavior Reveals
1298 a Tightly Coupled Stimulus-Response Loop. *Curr. Biol.* **30**, 54–69.e9 (2020).
- 1299 60. I. H. Bianco, A. R. Kampff, F. Engert, Prey Capture Behavior Evoked by Simple Visual Stimuli in Larval Zebrafish.
1300 *Front. Syst. Neurosci.* **5**, 101 (2011).
- 1301 61. M. Takechi, T. Hamaoka, S. Kawamura, Fluorescence visualization of ultraviolet-sensitive cone photoreceptor
1302 development in living zebrafish. *FEBS Lett.* **553**, 90–94 (2003).
- 1303 62. G. Salbreux, L. K. Barthel, P. A. Raymond, D. K. Lubensky, Coupling Mechanical Deformations and Planar Cell
1304 Polarity to Create Regular Patterns in the Zebrafish Retina. *PLoS Comput. Biol.* **8**, e1002618 (2012).
- 1305 63. S. C. Suzuki, A. Bleckert, P. R. Williams, M. Takechi, S. Kawamura, R. O. L. L. Wong, Cone photoreceptor types in
1306 zebrafish are generated by symmetric terminal divisions of dedicated precursors. *Proc. Natl. Acad. Sci.* **110**, 15109–
1307 15114 (2013).
- 1308 64. K. M. Kwan, E. Fujimoto, C. Grabher, B. D. Mangum, M. E. Hardy, D. S. Campbell, J. M. Parant, H. J. Yost, J. P.
1309 Kanki, C.-B. Chien, The Tol2kit: A multisite gateway-based construction kit for Tol2 transposon transgenesis
1310 constructs. *Dev. Dyn.* **236**, 3088–3099 (2007).

- 1311 65. A. Suli, A. D. Guler, D. W. Raible, D. Kimelman, A targeted gene expression system using the tryptophan repressor in
1312 zebrafish shows no silencing in subsequent generations. *Development*. **141**, 1167–74 (2014).
- 1313 66. T. Tsujimura, A. Chinen, S. Kawamura, Identification of a locus control region for quadruplicated green-sensitive opsin
1314 genes in zebrafish. *Proc. Natl. Acad. Sci. U. S. A.* **104**, 12813–12818 (2007).
- 1315 67. M. C. Halloran, M. Sato-Maeda, J. T. Warren, F. Su, Z. Lele, P. H. Krone, J. Y. Kuwada, W. Shoji, Laser-induced gene
1316 expression in specific cells of transgenic zebrafish. *Development* (2000).
- 1317 68. S. Chamberland, H. H. Yang, M. M. Pan, S. W. Evans, S. Guan, M. Chavarha, Y. Yang, C. Salesse, H. Wu, J. C. Wu,
1318 T. R. Clandinin, K. Toth, M. Z. Lin, F. St-Pierre, Fast two-photon imaging of subcellular voltage dynamics in neuronal
1319 tissue with genetically encoded indicators. *Elife* (2017), doi:10.7554/eLife.25690.
- 1320 69. C. A. Chapot, C. Behrens, L. E. Rogerson, T. Baden, S. Pop, P. Berens, T. Euler, T. Schubert, Local Signals in Mouse
1321 Horizontal Cell Dendrites. *Curr. Biol.* (2017), doi:10.1016/j.cub.2017.10.050.
- 1322 70. T. Baden, P. Berens, K. Franke, M. Roman-Roson, M. Bethge, Euler, The functional diversity of mouse retinal
1323 ganglion cells. *Nature*, 1–21 (2016).
- 1324 71. T. Yoshimatsu, P. R. P. R. Williams, F. D. F. D. D'Orazi, S. C. Suzuki, J. M. Fadool, W. T. T. Allison, P. A. P. A.
1325 Raymond, R. O. R. O. Wong, Transmission from the dominant input shapes the stereotypic ratio of photoreceptor
1326 inputs onto horizontal cells. *Nat. Commun.* **5**, 3699 (2014).
- 1327 72. A. Cardona, S. Saalfeld, J. Schindelin, I. Arganda-Carreras, S. Preibisch, M. Longair, P. Tomancak, V. Hartenstein, R.
1328 J. Douglas, TrakEM2 Software for Neural Circuit Reconstruction. *PLoS One*. **7**, e38011 (2012).
- 1329 73. J. Oesterle, C. Behrens, C. Schröder, T. Herrmann, T. Euler, K. Franke, R. G. Smith, G. Zeck, P. Berens, Bayesian
1330 inference for biophysical neuron models enables stimulus optimization for retinal neuroprosthetics. *Elife*. **9**, 1–38
1331 (2020).
- 1332 74. S. N. Wood, *Generalized additive models: an introduction with R* (CRC press, 2017).
- 1333 75. T. Baden, T. Euler, P. Berens, Understanding the retinal basis of vision across species. *Nat. Rev. Neurosci.* **21**, 5–20
1334 (2020).
- 1335 76. K. Franke, P. Berens, T. Schubert, M. Bethge, T. Euler, T. Baden, Inhibition decorrelates visual feature
1336 representations in the inner retina. *Nature*. **542**, 439–444 (2017).
- 1337 77. V. I. Govardovskii, N. Fyhrquist, T. Reuter, D. G. Kuzmin, K. Donner, In search of the visual pigment template. *Vis.*
1338 *Neurosci.* (2000), doi:10.1017/S0952523800174036.
- 1339 78. A. Chinen, T. Hamaoka, Y. Yamada, S. Kawamura, Gene duplication and spectral diversification of cone visual
1340 pigments of zebrafish. *Genetics*. **163**, 663–675 (2003).